Available online at www.sciencedirect.com
ScienceDirect
Polar Science 3 (2009) 31–55
http://ees.elsevier.com/polar/

High-temperature annealing of amoeboid olivine aggregates: Heating experiments on olivine–anorthite mixtures

Mutsumi Komatsu [a,*], Takashi Mikouchi [b], Masamichi Miyamoto [b]

[a] *The University Museum, University of Tokyo, 7-3-1 Hongo Bunkyo-ku, Tokyo 113-0033, Japan*
[b] *Department of Earth and Planetary Science, Graduate School of Science, University of Tokyo, 7-3-1 Hongo, Bunkyo-ku, Tokyo 113-0033, Japan*

Received 21 January 2008; revised 18 December 2008; accepted 4 March 2009
Available online 17 April 2009

Abstract

Amoeboid olivine aggregates (AOAs) are composed of forsteritic olivine, Fe,Ni-metal, and Ca,Al-rich nodules consisting mainly of Al-diopside, spinel, and anorthite. Although the textures, shapes, and mineralogy of AOAs are consistent with their being aggregates of nebular condensates, some textures are in conflict with equilibrium condensation calculations, indicating that AOAs were not produced by a simple one-stage condensation. To examine the origin of the constituent minerals within AOAs and their textural relationships, we performed heating experiments using mineral mixtures analogous to those in AOAs. Isothermal and cooling experiments on forsterite + anorthite mixtures reveal that a high-Ca pyroxene phase forms via the incipient melting of the two minerals. Comparative studies of heating experiments performed using the mineralogy of AOAs suggest that Al-diopside in AOAs can be produced from a small degree of melting of forsterite and anorthite. The formation of Al-diopside in this way is consistent with the annealing textures observed in AOAs, and it may account for the discrepancy between the observed mineralogy of AOAs and the results of equilibrium condensation calculations, the occurrence of two types of diopside (Al,Ti-rich diopside and Al-diopside), and the variable Al_2O_3 content of Al-diopside.

Keywords: Carbonaceous chondrites; CAIs; Amoeboid olivine aggregates; Heating experiments

1. Introduction

Amoeboid olivine aggregates (AOAs) are irregularly shaped objects (several tens of microns to 1 cm in size) composed of olivine, Al-diopside, feldspar, and spinel ± melilite, ±perovskite, ±Fe,Ni-metal, ±feldspathoids, and ±sulfides, and are found in several carbonaceous chondrite groups (Bar-Matthews et al., 1979; Chizmadia and Rubin, 2000; Cohen et al., 1983; Grossman and Steele, 1976; Hashimoto and Grossman, 1987; Komatsu et al., 2001; Kornacki and Wood, 1984a,b; Krot et al., 2004a; Lin and Kimura, 2003; McSween, 1977; Rubin, 1998; Sugiura et al., 2006; Weisberg et al., 2004).

Based on detailed mineralogical, petrographic, and chemical studies of AOAs, largely of the oxidized CV chondrite Allende and thermodynamic analysis, it has been suggested that these objects are aggregates of solar nebular condensates (forsterite, Al-diopside, and spinel) that continued to react with the solar nebular vapor to form anorthite, ilmenite, nepheline, sodalite,

* Corresponding author.
E-mail address: mutsumi@um.u-tokyo.ac.jp (M. Komatsu).

1873-9652/$ - see front matter © 2009 Elsevier B.V. and NIPR. All rights reserved.
doi:10.1016/j.polar.2009.03.002

salite-hedenbergitic pyroxenes, andradite, fayalitic olivine, sulfides, and phyllosilicates (Grossman and Steele, 1976; Hashimoto and Grossman, 1987). Later studies demonstrated that AOAs in primitive carbonaceous chondrites consist of forsterite, Fe,Ni-metal, and Ca,Al-rich inclusions composed of Al-diopside, spinel, anorthite, and rare melilite (Krot et al., 2004a). Krot et al. (2004a) concluded that AOAs are aggregates of solar nebular condensates composed of forsterite, Fe,Ni-metal, and CAIs, and that secondary alteration resulted in the formation of phyllosilicates, magnetite, carbonates, nepheline, sodalite, grossular, wollastonite, hedenbergite, andradite, and ferrous olivine.

However, AOAs possess several unique textures that are inconsistent with equilibrium condensation calculations, indicating that they were not produced by simple one-stage condensation. The observation that anorthite is rimmed by Al-diopside, which in turn is rimmed by olivine (which is supposed to have originally been forsterite), is in conflict with equilibrium condensation calculations that predict that forsterite should condense prior to anorthite, depending on nebular pressure (e.g., Petaev and Wood, 2005).

Based on a mineralogical study of reduced CV3 chondrites, we found several textures that indicate AOAs have experienced high-temperature nebular processing, including annealing and incipient melting, and were subsequently isolated from high-temperature nebular gas, possibly by physical removal (e.g., Cuzzi and Zahnle, 2004; Shu et al., 2001). Annealing and a small degree of melting of AOAs are indicated by the presence of olivine triple-junction grain boundaries, ‘‘doughnut-shaped’’ forsterite, rounded Fe,Ni-metal nodules in some AOAs, and their relatively compact textures. To understand the thermal history of AOAs subsequent to their aggregation, we performed isothermal heating and cooling experiments involving the constituent minerals within AOAs.

2. Methods

2.1. Petrographic examination and chemical analyses

Polished thin sections of four CV3 chondrites (Efremovka, Leoville, Vigarano, and Allende) were studied under reflected and transmitted light using optical microscopy, and were mapped in terms of Ca, Al, Mg, Ti, and Na concentrations using Kα X-rays with a resolution of approximately 5–10 μm (2 μm for individual AOAs) using a Cameca SX-50 electron microprobe at the Hawaii Institute of Geophysics and Planetology, University of Hawaii, and a JEOL JXA 8900L microprobe at the Department of Earth and Planetary Science, University of Tokyo. Identified AOAs were studied in back-scattered electron (BSE) images obtained using a Hitachi S-4500 field emission gun SEM equipped with energy dispersive spectrometers (EDSs), using KEVEX SIGMA analysis systems at the Department of Earth and Planetary Science, University of Tokyo. Quantitative analyses were performed using the SX-50 electron microprobe at the University of Hawaii and a JEOL JCM 733 mk II electron microprobe at the University of Tokyo, operated at 15 kV and 20 nA. Analyses with totals below 96 wt% or above 103 wt% were excluded from consideration. Counting times at peak wavelength were 40 s. The background intensity of each element was counted on both sides of the peak wavelength.

Approximate standard deviations based on counting statistics for focused beam analyses of silicates are as follows (in wt%): SiO_2, 0.30; TiO_2, 0.04; Al_2O_3, 0.10; Cr_2O_3, 0.05; FeO, 0.14; MnO, 0.05; MgO, 0.19; CaO, 0.06; Na_2O, 0.06; and K_2O, 0.02.

2.2. Heating experiments

Heating experiments were performed to examine the relationships among constituent minerals in AOAs during high-temperature processing. Starting materials were mixtures of terrestrial anorthite (Miyakejima, Tokyo, Japan; $An_{95}Ab_5$) and olivine (San Carlos, Arizona, USA; Fo_{92}) or synthetic forsterite (Fo100) (Table 1). Small rock chips used as starting material were ground to pass through a 100 μm sieve and a 37 μm sieve. Pellets were pressed from ~100 mg of starting mix, sintered onto loops (~5 mm diameter) fabricated from Pt-wire (0.2 mm in diameter), and

Table 1
Chemical compositions of minerals used for starting materials.

	Olivine	anorthite	forsterite
SiO_2	40.3	44.0	42.4
Al_2O_3	0.01	35.1	0.03
TiO_2	0.01	0.02	0.01
FeO	8.58	0.53	0.02
MnO	0.14	0.03	0.03
MgO	49.5	0.09	57.5
CaO	0.08	19.1	0.02
Na_2O	0.01	0.57	0.01
K_2O	0.01	0.01	0.01
Cr_2O_3	0.02	0.02	0.02
V_2O_3	0.02	0.01	0.01
NiO	0.40	0.02	0.01
Total	99.1	99.4	100.0

suspended from a ceramic tube at the hotspot of the vertical furnace. An appropriate mixture of H_2 and CO_2 gases was passed through the furnace to achieve the desired fO_2. Two pellets were placed in the furnace at a time, yielding multiple charges from the same experimental run. Experimental temperatures were measured using Pt–$Pt_{90}Rh_{10}$ thermocouples whose junctions were within 5 mm of the experimental charges in the furnace. Thermocouples were calibrated against the melting point of gold (1064 °C).

Because carbonaceous chondrite is known to have an intrinsic oxygen fugacity near the IW (iron wüstite) buffer (Brett and Sato, 1984), it is appropriate to consider that heating of AOAs occurred under similar redox conditions. Therefore, heating experiments were performed under the oxygen fugacity of IW. Experiments were also performed at the QFM (quartz–fayalite–magnetite) buffer and under atmospheric conditions (more oxidized than IW) to assess the effect of varying oxygen fugacity.

The aim of this study was to examine the mineralogy of samples at the desired temperature. After reaching the final run temperature, samples were held for 3, 15, 50, and 100 h, then air-quenched by pulling the sample-support rod out of the furnace. The samples were then made into polished sections to be examined under the microscope and from which to measure the chemical composition using a JEOL JXA 8900L microprobe.

Cooling experiments were performed to investigate the effect of heating and cooling conditions. The samples were heated at temperatures that caused incomplete melting for 3 h, then cooled at various cooling rates (10–500 °C/h) to 900 °C, at which point the charges were quenched. The experimental conditions for the isothermal and cooling experiments are listed in Tables 2a and 2b.

Table 2a
Experimental conditions and phases present in run product.

Run no.	T (°C)	Proportion oxygen fugacity	heating	duration	Size (μm)	Phases present
Olivine–anorthite (ol:an)						
1	Unheated	1:1	–	–	–	ol, an
2	1243	1:1	IW	3 h	<37	ol, an
3	1268	1:1	IW	3 h	<37	ol, an
4	1268	1:1	IW	15 h	<37	ol, an
5	1276	1:1	IW	3 h	<37	ol, an
6	1276	1:1	IW	15 h	<37	ol, an
7	1288	1:1	IW	3 h	<37	ol, an, cpx, sp
8	1288	1:1	IW	15 h	<37	ol, an, cpx, sp
9	1288	1:1	IW	50 h	<37	ol, an, cpx, sp
10	1288	1:1	IW	100 h	<37	ol, an, cpx, sp
11	1288	1:1	QFM	15 h	<37	ol, an, cpx, sp
12	1288	1:1	Air	3 h	<37	ol, an, cpx, sp
13	1301	1:1	IW	3 h	<37	ol, gl, sp
14	1313	1:1	IW	3 h	<37	ol, gl, sp
15	1313	1:1	IW	15 h	<37	ol, gl, sp
16	1337	1:1	IW	3 h	<37	ol, gl, sp
17	1438	1:1	IW	1 h	<37	ol,gl
18	1288	9:1	IW	3 h	<37	ol, cpx, sp
19	1288	4:1	IW	3 h	<37	ol, an, cpx, sp
20	1337	4:1	IW	3 h	<37	ol, an, cpx, sp
21	1288	7:3	IW	3 h	<37	ol, an, cpx, sp
22	1288	6:4	IW	3 h	<37	ol, an, cpx, sp
23	1288	1:1	IW	3 h	< 100	ol, an, cpx, sp
24	1438	1:1	IW	3 h	< 100	ol,gl
25	1278	4:1	IW	1 h	< 100	ol, an
26	1283	4:1	IW	1 h	< 100	ol, an, cpx, sp
27	1293	4:1	IW	1 h	< 100	ol, gl, sp
28	1298	4:1	IW	1 h	< 100	ol, gl, sp
Forsterite–anorthite (fo:an)						
29	1298	1:1	IW	3 h	< 100	fo, an
30	1308	1:1	IW	3 h	< 100	fo, an, cpx, sp
31	1313	1:1	IW	3 h	< 100	fo, an, cpx, sp
32	1313	1:1	IW	20 h	< 100	fo, an, cpx, sp
33	1318	1:1	IW	3 h	< 100	fo, an, cpx, sp
34	1337	1:1	IW	3 h	< 100	fo, gl, sp
35	1298	4:1	IW	1 h	< 100	fo, an
36	1308	4:1	IW	3 h	< 100	fo, an, cpx, sp
37	1313	4:1	IW	3 h	< 100	fo, an, cpx, sp
38	1313	4:1	IW	20 h	< 100	fo, an, cpx, sp
39	1318	4:1	IW	3 h	< 100	fo, an, cpx, sp

2.3. Electron back-scattering diffraction patterns

Electron back-scattering diffraction (EBSD) analysis was employed to study the crystallography of AOA minerals, using a phase-ID EBSD system (NORAN instruments Inc., Japan) equipped to JEOL JXA 840 and Hitachi S-4500 SEMs. The accelerating voltage of the incident electrons was 20 kV and the beam current was in the range of several nanoampere. The collection semi-angle of the EBSD detector was about 37.5°. The specimens were coated with amorphous carbon (several tens of nanometers thick) before analysis to ensure appropriate electrical conductivity. The specimens were tilted by about 70° from the horizon toward the phosphor screen (the detector) using a custom-made specimen mount. The Kikuchi band, a pair of dark lines separated by $2\theta_{hkl}$ (where θ_{hkl} is the Bragg angle of the lattice plane with an index of *hkl)* and for which the area inside the two lines is brighter than the lines themselves, was determined by dynamical calculation (Dudarev et al., 1995; Spencer et al., 1972). Simulations of the EBSD patterns were performed using a program coded using Visual Basic 6.0, as developed by Kogure (2003).

Table 2b
Experimental conditions of cooling experiments.

Run no.	Olivine	Forsterite	Anorthite	T (°C)	Cooling rate (°C/h)
1	–	1	1	1300	50
2	–	1	1	1305	500
3	–	1	1	1308	10
4	–	1	1	1308	50
5	–	1	1	1308	500
6	–	1	1	1313	Quench
7	–	1	1	1313	10
8	–	1	1	1313	20
9	–	1	1	1313	50
10	–	1	1	1313	100
11	–	1	1	1313	500
12	–	1	1	1320	10
13	–	1	1	1320	300
14	–	1	1	1320	500
15	–	1	1	1335	50
16	–	1	1	1337	10
17	–	1	1	1337	500
18	–	1	1	1350	100
19	–	1	1	1357	10
20	–	1	1	1357	100
21	–	1	1	1357	500
22	–	1	1	1360	50
23	–	1	1	1410	50
24	–	4	1	1303	50
25	–	4	1	1308	10
26	–	4	1	1308	50
27	–	4	1	1313	10
28	–	4	1	1313	20
29	–	4	1	1313	50
30	–	4	1	1313	100
31	–	4	1	1313	500
32	–	4	1	1320	10
33	–	4	1	1320	300
34	–	4	1	1320	500
35	–	4	1	1335	50
36	–	4	1	1337	10
37	–	4	1	1337	500
38	–	4	1	1350	100
39	–	4	1	1357	10
40	–	4	1	1357	500
41	–	4	1	1360	50
42	–	4	1	1370	100
43	–	4	1	1410	50
44	1		1	1350	10
45	1		1	1288	100
46	4		1	1288	100
47	–	1	1	1310	500
48	–	1	1	1320	10
49	–	1	1	1320	500
50	–	4	1	1310	500
51	–	4	1	1320	10
52	–	4	1	1320	500
53	–	1	1	1320	500
54	–	1	1	1357	100
55	–	4	1	1320	500

3. Results

3.1. Petrographic examination of reduced CV chondrites

AOAs from the reduced CV chondrites Efremovka, Leoville, and Vigarano are irregularly shaped objects (up to 5 mm in size) composed of anhedral, fine-grained forsteritic olivine (5–20 μm) and refractory Ca,Al-rich components; low-Ca pyroxene was not observed (Fig. 1a and b). The Ca,Al-rich components, which consist of fine-grained Mg-rich spinel, Al-diopside, and anorthite, are characterized by significant variations in size (1–250 μm), distribution (from uniform to heterogeneous), modal mineralogy (from spinel-rich to spinel-poor), and abundance (from rare to abundant).

Two types of Al-diopside occur in the AOAs: Al-diopside (generally 0–17 wt% Al_2O_3 and <3 wt% TiO_2) typically overgrows forsterite, whereas Al,Ti-rich diopside (generally 20–30 wt% Al_2O_3 and 7–10 wt% TiO_2) is associated with spinel (Fig. 1c).

The AOAs contain textures that indicate heating subsequent to aggregation. Al-diopside and anorthite are occasionally mantled by a thick shell of forsteritic olivine (Fig. 1e) or forsteritic olivine with triple-junction grain boundaries (Fig. 1d). These objects are similar to ‘‘doughnut-shaped’’ olivine in AOAs reported previously from Allende (Bar-Matthews et al., 1979). Some Al-diopside–anorthite regions contain rounded nodules of Fe,Ni-metal, Ti-rich Al-diopside, andtroilite (Fig. 1c).

Most AOAs from the reduced CV chondrites Efremovka, Leoville, and Vigarano contain few secondary minerals. The magnesian composition of olivine and spinel in reduced CV3 chondrites, combined with a lack of secondary minerals in AOAs, indicates that the AOAs experienced a significantly lower degree of alteration than did those from the oxidized CV chondrite Allende (Fig. 1f, Table 3). This finding indicates in turn that the AOAs were originally forsteritic olivine, anorthite, Al-diopside, spinel, perovskite, melilite, and metal, altered to Fe-containing olivine, nepheline, and sodalite. In addition to this alteration, it is possible that the AOAs experienced thermal processing.

3.2. Heating experiments

The most characteristic feature of Ca,Al-rich nodules is that spinel and anorthite cores are surrounded by Al-diopside, which overgrows olivine

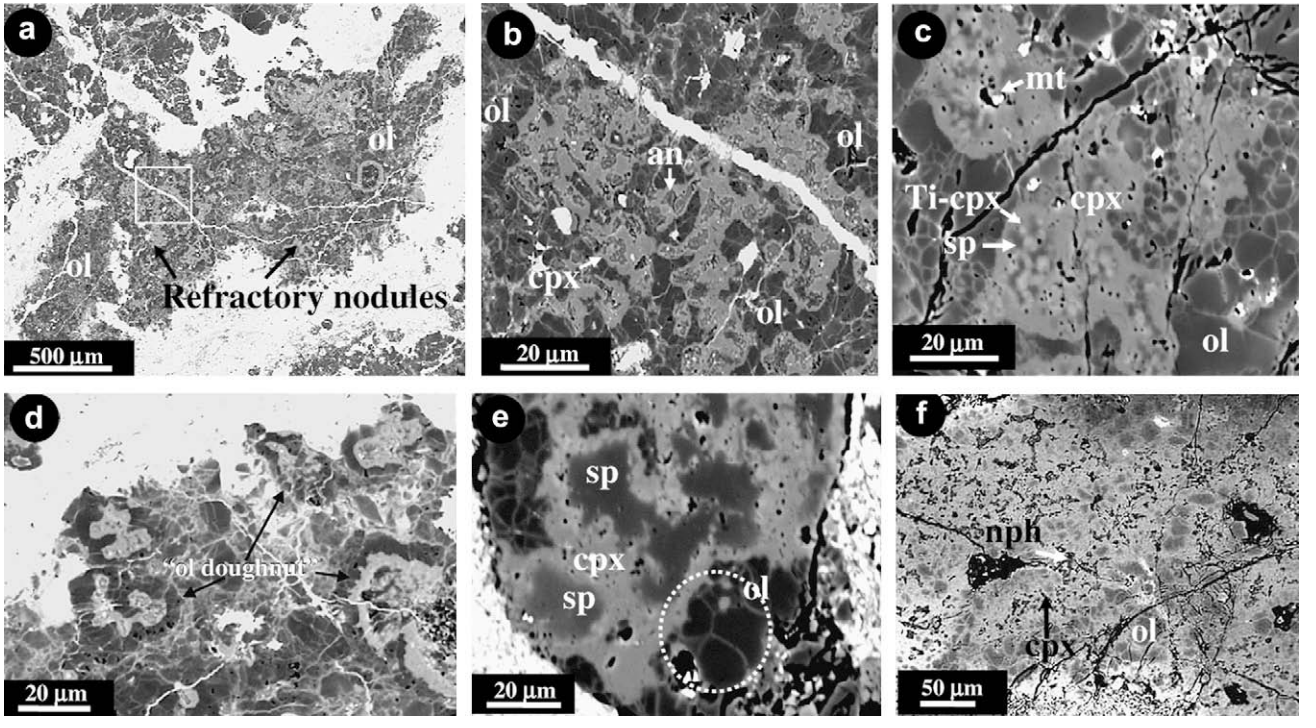

Fig. 1. Back-scattered electron (BSE) images of AOAs from (a, b) Leoville, (c) Efremovka, (d, e) Vigarano, and (f) Allende. Refractory inclusions in AOAs are typically zoned, consisting of cores of spinel and anorthite, and rims of Al-diopside. Anorthite is partially replaced by nepheline and sodalite in altered AOAs. The square in (a) corresponds to (b). The dotted oval in (e) shows the triple-junction grain boundaries of olivine.ol: olivine, cpx: Al-diopside, Ti-cpx: Al,Ti-diopside, an: anorthite, sp: spinel, nph: nepheline, mt: Fe,Ni-metal.

Table 3
Representative microprobe analyses of primary minerals in AOAs from CV chondrites.

	Reduced CVs					Oxidized CVs	
	Vigarano AOA				Leoville	Allende AOA	
	Al,Ti-diopside	Al-diopside	Olivine	Spinel	Anorthite	Olivine	Al-diopside
SiO_2	36.6	48.6	42.5	0.12	41.7	40.3	47.7
TiO_2	7.13	0.31	<0.04	0.23	0.07	0.04	1.54
Al_2O_3	21.8	11.9	<0.04	70.4	36.1	0.33	11.6
Cr_2O_3	0.06	0.13	0.05	0.44	<0.05	0.14	0.14
FeO	0.24	0.32	2.13	4.26	1.33	15.9	1.75
MnO	<0.07	<0.07	<0.07	<0.07	<0.07	0.07	<0.07
MgO	9.17	14.9	55.8	25.9	1.29	43.5	14.7
CaO	24.3	25.0	0.15	0.16	19.3	0.17	23.5
Na_2O	<0.04	<0.04	<0.04	<0.04	<0.04	0.09	0.69
K_2O	<0.05	<0.05	<0.05	<0.05	<0.05	<0.05	0.09
Total	99.3	101.1	100.7	101.5	99.8	100.5	101.8
Fa	–	–	2.1	–	–	17.0	–
Fs	0.5	0.6	–	–	–	–	–
An	–	–	–	–	100.0	–	–

(Fig. 1b and c). To investigate the textural relationships among spinel, anorthite, Al-diopside, and olivine, we performed isothermal and cooling experiments on mixtures of terrestrial olivine (Fo_{92}), anorthite (An_{95}), and synthetic forsterite.

3.2.1. Isothermal experiments on San Carlos olivine and Miyakejima anorthite

We performed a series of isothermal experiments on San Carlos olivine and Miyakejima anorthite. With increasing heating temperature during the experiments, olivine and anorthite gradually reacted with each other at grain rims. The obtained anorthite texture reveals that the rims started melting at 1263 °C, filling the space between olivine grains (Fig. 2b). The melting of anorthite is more advanced in the sample heated at 1276 °C (Fig. 2c). In contrast to anorthite, olivine still shows sharp grain boundaries, suggesting that it did not melt or react with anorthite at temperatures lower than 1276 °C. At 1288 °C, olivine grain boundaries become less distinct, and a new phase (with high-Ca pyroxene stoichiometry) appears around olivine rims (Fig. 2d). The new phase only appears between olivine and anorthite, with widths of 2–10 μm in the <37 urn sample and 5–20 μm in the < 100 μm sample. EBSD analysis of this high-Ca pyroxene phase reveals an amorphous structure. It should be noted that the heating duration (3, 15, 50, and 100 h) shows no relationship with the degree of melting; thus, it seems that reactions at the experimental temperatures were completed in less than 3 h. Spherical spinel grains (<10 μm) were also observed.

The sample heated at 1288 °C shows similar textures to those of AOAs (Fig. 1b), including distinct grain boundaries between anorthite and high-Ca pyroxene glass, and obscure grain boundaries between olivine and high-Ca pyroxene glass. These textures suggest that both Al-diopside in AOAs and high-Ca pyroxene glass in the charges may have formed via a reaction between olivine and anorthite during heating. Anorthite is completely melted at a temperature of 1301 °C (Fig. 2e). At 1438 °C, most of the anorthite and olivine grains are extensively melted: only relic olivine and the glassy high-Ca phase are observed (Fig. 2f).

To examine the relationships between the amount of high-Ca pyroxene glass and relative abundance of olivine, heating experiments were conducted at 1288 °C with various ratios of olivine to anorthite (Fig. 3). The heated charge with initial olivine:anorthite = 9:1 yields high-Ca pyroxene glass (5–20 μm in width) and no remaining anorthite (Fig. 3a). Both olivine and anorthite are present in the samples with initial olivine:anorthite = 4:1, in which the high-Ca pyroxene glass is 5–15 μm in width (Fig. 3b). The width of high-Ca pyroxene glass decreases with increasing amount of anorthite, indicating that the formation of high-Ca pyroxene glass (via a reaction between olivine with anorthite) depends on the ratio of olivine to anorthite in the starting material.

As shown in Table 4, the sample with olivine:anorthite = 4:1 has a bulk composition similar to that of AOAs from reduced CV chondrites. Therefore,

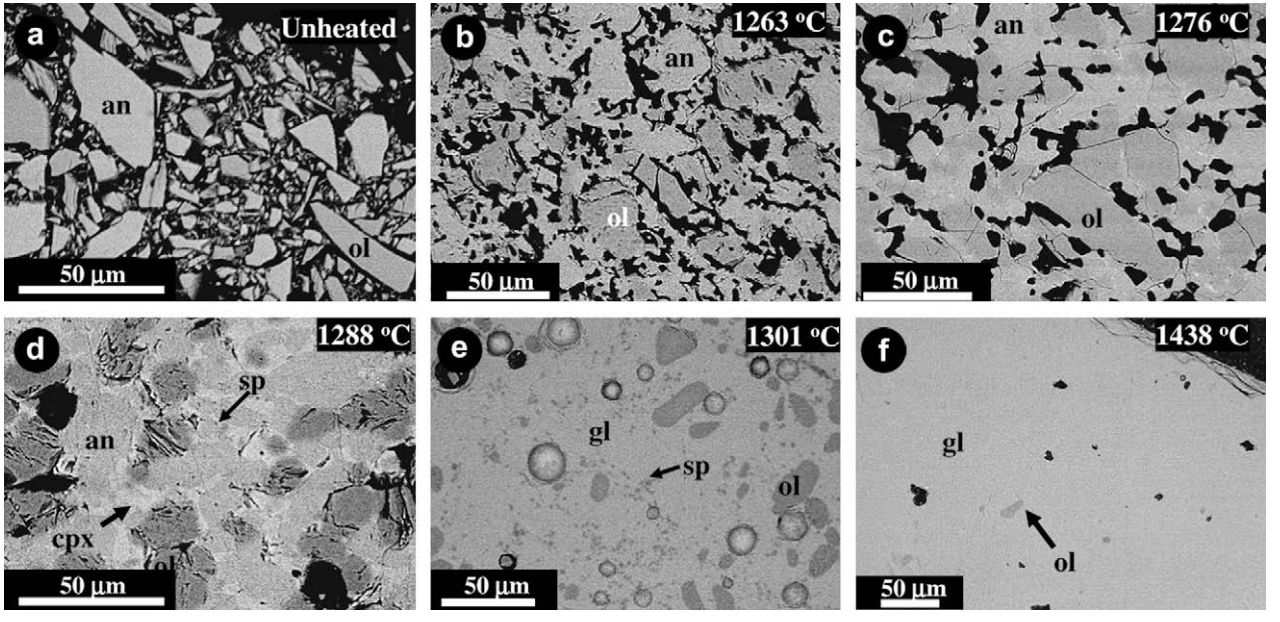

Fig. 2. Textural changes in olivine (Fo_{92}) and anorthite ($An_{95}Ab_5$) with increasing heating temperature (isothermal experiments), heated for 3 h under the oxygen fugacity of IW. With increasing annealing temperature, olivine and anorthite gradually react from their rims inward, and high-Ca pyroxene glass is observed in samples heated above 1288 °C. ol: olivine, an: anorthite, cpx: high-Ca pyroxene glass, sp: spinel, gl: glass.

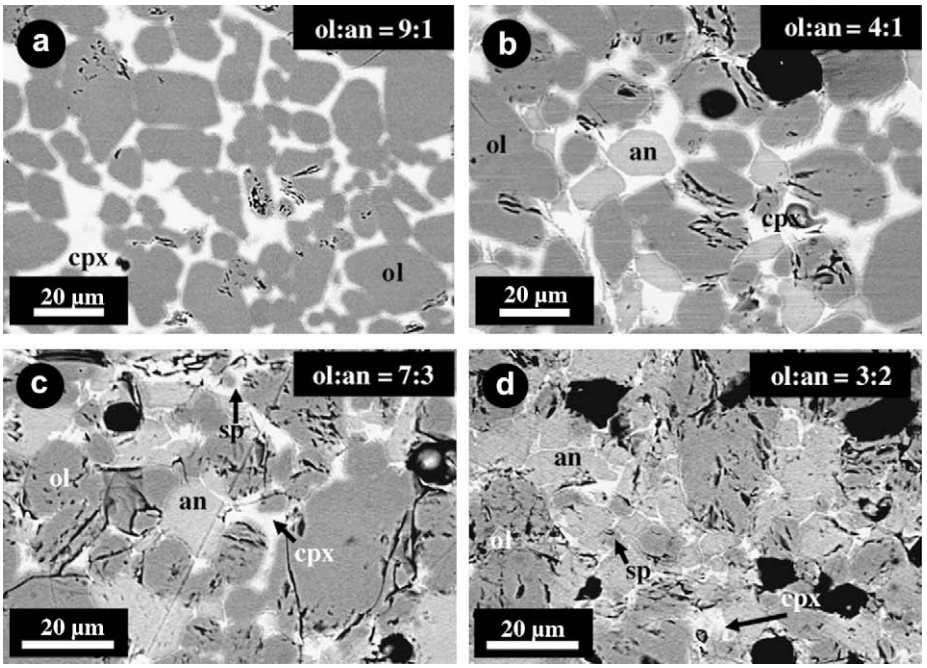

Fig. 3. BSE images of samples heated at 1288 °C. The size of high-Ca pyroxene glass decreases with increasing olivine in the starting material. ol: olivine, an: anorthite, cpx: high-Ca pyroxene glass.

heating experiments were performed at several different temperatures with olivine:anorthite = 4:1 (Fig. 4). A high-Ca pyroxene glass occurs at 1283 °C via a reaction between olivine and anorthite. Although the amount of glass is less than that in samples with olivine:anorthite = 1:1, its mode of occurrence is the same in both cases. The texture of the high-Ca pyroxene glass is similar to that of Al-diopside in natural AOAs. Anorthite is completely melted at 1293 °C (Fig. 4b). Thus, the heating experiments produce textures similar to those of natural AOAs over a narrow temperature range (<10 °C) near 1288 °C, and over a wide range of starting materials (olivine:anorthite ratios of between 1:1 and 4:1). It is also noted that larger grains of high-Ca pyroxene glass formed in experiments with coarser starting materials.

Although we performed some experiments at 1288 °C under QFM conditions, we found no clear

Table 4
Calculated bulk compositions of olivine + anorthite mixture, and bulk compositions of AOAs from reduced CV chondrites.

	Olivine + anorthite mixure[a]						AOA		
	ol:an = 1:1	ol:an = 3:2	ol:an = 7:3	**ol:an = 4:1**	ol:an = 9:1	fo:an = 1:1	Leoville #36	Leoville #7	Efremovka #8
SiO_2	42.2	41.8	41.4	41.1	40.7	43.2	43.6	41.4	39.6
Al_2O_3	17.5	14.0	10.5	7.02	3.52	17.5	4.30	7.61	3.82
TiO_2	0.02	0.02	0.02	0.01	0.01	0.00	0.19	0.36	0.13
FeO	4.56	5.36	6.17	6.97	7.78	0.30	4.32	4.63	11.2
MnO	0.08	0.09	0.10	0.11	0.12	0.00	0.16	0.17	0.15
MgO	24.8	29.7	34.7	39.6	44.5	28.8	43.1	39.6	42.5
CaO	9.60	7.69	5.79	3.89	1.99	9.60	4.01	5.86	2.24
Na_2O	0.29	0.24	0.18	0.13	0.07	0.30	0.03	0.08	0.08
K_2O	0.01	0.01	0.01	0.01	0.01	0.00	0.01	0.02	0.01
Cr_2O_3	0.02	0.02	0.02	0.02	0.02	0.00	0.27	0.24	0.34
V_2O_3	0.01	0.02	0.02	0.02	0.02	0.00	0.00	0.00	0.00
NiO	0.21	0.25	0.29	0.33	0.37	0.00	0.00	0.00	0.00
Total	99.3	99.2	99.2	99.2	99.1	99.7	100.0	100.0	100. 0

[a] Bulk compositional data are from Komatsu et al. (2001).

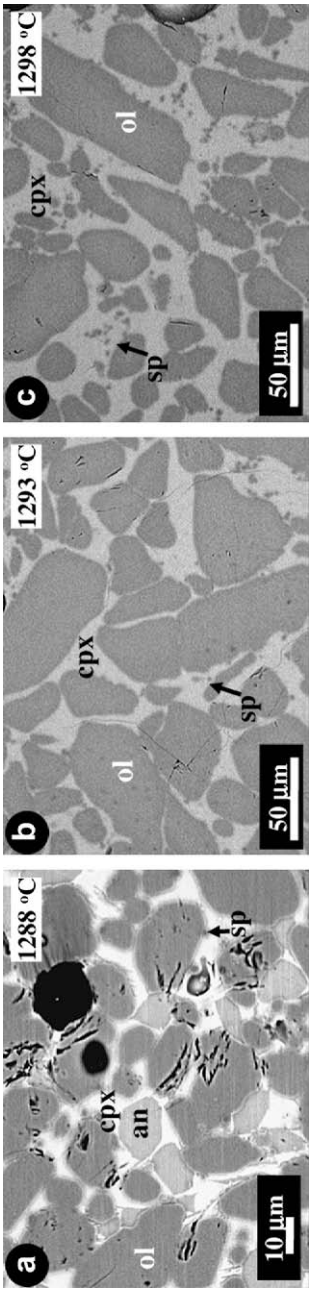

Fig. 4. BSE images of run products with olivine–anorthite = 4:1, heated at 1288,1293, and 1298 °C under IW conditions. A high-Ca pyroxene glass forms at 1283 °C from the reaction between olivine and anorthite. Although the amount of high-Ca pyroxene glass in the sample with olivine:anorthite = 4:1 is smaller than that in the sample with olivine:anorthite = 1:1, the mode of occurrence is the same in both cases. ol: olivine, an: anorthite, cpx: high-Ca pyroxene glass, sp: spinel.

textural difference between samples at the oxygen fugacities of QFM and IW; however, the charge heated at 1288 °C under atmospheric conditions showed a different texture from those heated at the same temperature under IW and QFM conditions. Anorthite is completely melted in the sample heated at 1288 °C under atmospheric conditions.

3.2.2. Isothermal experiments on forsterite + anorthite mixtures

Olivine in AOAs from reduced CVs has an average composition of Fo90–99 (Komatsu et al., 2001) Although it is known that AOAs in primitive carbonaceous chondrites contain near-pure forsterite (Krot et al., 2004a), to evaluate the Fa content of olivine in response to mineralogical changes caused by heating, we performed isothermal experiments on forsterite + anorthite mixtures.

Fig. 5 shows the textural changes that occur in mixtures of synthetic forsterite (Fo_{100}) and anorthite heated under the oxygen fugacity of IW. No textural changes were observed in samples heated at temperatures less than 1298 °C (Fig. 5a and b), but anorthite shows a small degree of melting at 1313 °C (Fig. 5c). There is no obvious change in the charges heated for 3 and 20 h. High-Ca pyroxene glass formed at higher temperatures. As with the olivine + anorthite mixtures, EBSD analysis revealed that the glass phase was amorphous. The grain boundaries between the high-Ca pyroxene glass and anorthite are less clear than those in the charges comprising an olivine (Fo92) + anorthite mixture. The high-Ca pyroxene glass is darker than anorthite in the BSE image, in contrast to the olivine + anorthite mixture. The degree of anorthite melting is extensive in the charge heated at 1318 °C, in which the grain boundaries between anorthite and the high-Ca pyroxene phase are difficult to recognize (Fig. 5d). At 1337 °C, anorthite is completely melted: only rounded forsterite grains and anorthositic glass are observed (Fig. 5e).

3.2.3. Cooling experiments on olivine and anorthite

The results of isothermal experiments show that a high-Ca pyroxene glass is produced by reactions between olivine/forsterite and anorthite. We performed cooling experiments on olivine and anorthite to assess the influence of the cooling rate after heating by observing the textures of high-Ca pyroxene in the charges.

Fig. 6 shows the textures of olivine + anorthite mixtures heated at 1288 °C and 1350 °C for 3 h under the IW condition and cooled at 10 and 100 °C/h.

High-Ca pyroxene and mesostasis are present in the heated charges. In contrast to the high-Ca pyroxene glass formed in isothermal experiments, the cooling experiments produced crystalline high-Ca pyroxene, as indicated by EBSD analyses (Fig. 7). It appears that the amount of high-Ca pyroxene and mesostasis is smaller in the charge heated at 1288 °C (Fig. 6a and b) than in the charge heated at 1350 °C (Fig. 6c). The isothermal experiment at 1288 °C resulted in incomplete melting of olivine and anorthite, whereas heating at 1350 °C led to the complete melting of anorthite. In addition, less high-Ca pyroxene is produced in the charges during cooling experiments than during isothermal experiments. These results indicate that olivine and anorthite recrystallized from the melt and overgrew relict olivine and anorthite grains, and that the amounts of high-Ca pyroxene and mesostasis depend on the amount of interstitial melt before cooling.

3.2.4. Cooling experiments on forsterite + anorthite mixtures

Fig. 8 shows textural changes in forsterite + anorthite mixtures for various cooling rates. The abundance of high-Ca pyroxene in forsterite + anorthite charges subjected to cooling experiments is generally lower than that in charges subjected to isothermal experiments.

In the forsterite:anorthite = 1:1 sample, the charges show no evidence of melting at 1300 °C. Anorthite starts melting at grain boundaries with forsterite at 1305 °C (Fig. 8a and b). These observations are consistent with the results of isothermal experiments (Fig. 5). At 1308 °C, a small amount of high-Ca pyroxene is observed. The high-Ca pyroxene is clearly observed in the charges heated at 1313 °C, occurring at anorthite grain boundaries (Fig. 8d) and occasionally surrounding forsterite. The charges heated at 1320 °C contain a number of lath-shaped anorthite crystals (~10 μm in width; Fig. 8e), suggesting that anorthite was largely melted at 1320 °C and that lath-shaped anorthite recrystallized from relict nuclei during cooling. Anorthite is completely melted at temperatures above 1337 °C (Fig. 8f), for which a large number of lath-shaped anorthite (2–10 μm in width) and high-Ca pyroxene (<3 μm in width) crystals are observed.

The textural changes observed in forsterite:anorthite = 4:1 charges with increasing heating temperature are similar to those observed in forsterite:anorthite = 1:1 charges (Fig. 8), although a smaller amount of high-Ca pyroxene is produced in the former charges compared with the latter.

The charges heated at 1313 °C with a slow cooling rate (10 °C/h; Fig. 10a) contain less high-Ca pyroxene than charges heated at higher temperatures and with fast cooling rates (e.g., 500 °C/h; Fig. 9d). Lath-shaped anorthite and high-Ca pyroxene are more prominent in rapidly cooled charges than in slowly cooled charges. The grain size of high-Ca pyroxene is larger in the charges cooled at 10 °C/h than in those cooled at 500 °C/h. These observations are true for all the cooling experiments.

3.3. Mineral chemistry of run products

3.3.1. Isothermal experiments

3.3.1.1. Olivine:anorthite = 1:1, heated under the oxygen fugacity of IW. Table 5 lists compositional data for olivine, anorthite, and high-Ca pyroxene glass. Although the high-Ca pyroxene glass in the quenched charges shows variable composition in individual samples, the average composition in each sample shows a systematic increase in MgO content with increasing temperature (from 12 wt% at 1288 °C to 21.8 wt% at 1438 °C), decrease in SiO_2 content (from 46.6 wt% at 1288 °C to 42.7 wt% at 1438 °C), and decrease in CaO content (from 13.3 wt% at 1288 °C to 10.9 wt% at 1438 °C). Although the total cation values of the high-Ca pyroxene glass and glassy phase show a slight increase with increasing annealing temperature, all the values fall around 4.0 ($O = 6$), consistent with the stoichiometry of high-Ca pyroxene (Table 5). The high-Ca pyroxene glass heated at 1288 °C is closest to the stoichiometric composition of high-Ca pyroxene.

Table 6 lists the compositional changes that occur with increasing duration of heating. Fe was absorbed by Pt-wire during the heating experiments, resulting in a decrease in the average FeO content in olivine (from 7.5 to 5.2 wt%) in the samples heated at 1288 °C for 100 h. Except for the FeO content in olivine, there is no clear difference in composition between the samples heated for 3 and 100 h. Although the high-Ca pyroxene glass in the charge heated for 100 h shows a higher MgO content than the charge heated for 3 h, the MgO content of high-Ca pyroxene remains highly variable among the different heating durations.

3.3.1.2. Olivine:anorthite = 9:1 to 3:2, heated at 1288 °C under the oxygen fugacity of IW. Table 7 lists the results of heating experiments performed at 1288 °C with various olivine:anorthite ratios. High-Ca

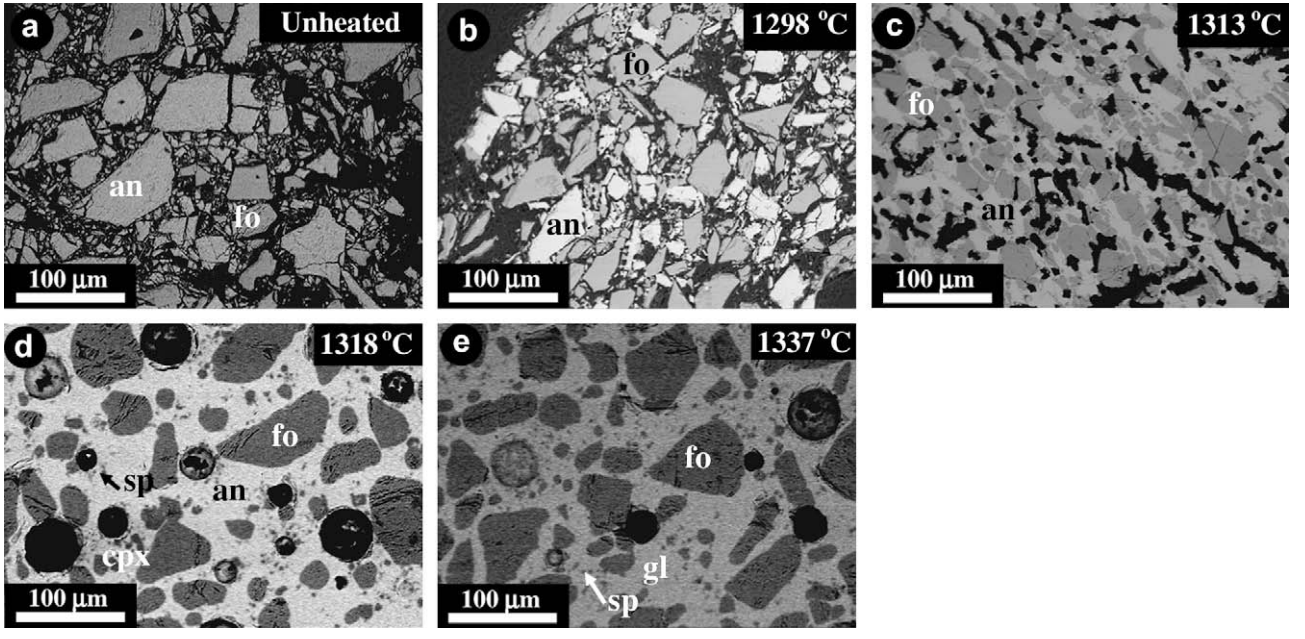

Fig. 5. Textural changes in mixtures of synthetic forsterite (Fo_{100}) and anorthite ($An_{95}Ab_5$) with increasing heating temperature (isothermal experiments) under the oxygen fugacity of IW. (a) Unheated sample. (b) Only little evidence of melting is observed at 1298 °C. (c) Anorthite shows a small degree of melting at 1313 °C, and a high-Ca pyroxene glass is produced. (d) Extensive anorthite melting is observed in the charge heated at 1318 °C, and the grain boundaries between anorthite and high-Ca pyroxene glass become obscure. (e) Anorthite is completely melted at 1337 °C, and only rounded forsterite grains and anorthositic glass are observed. fo: forsterite, an: anorthite, cpx: high-Ca pyroxene glass, sp: spinel, gl: glass.

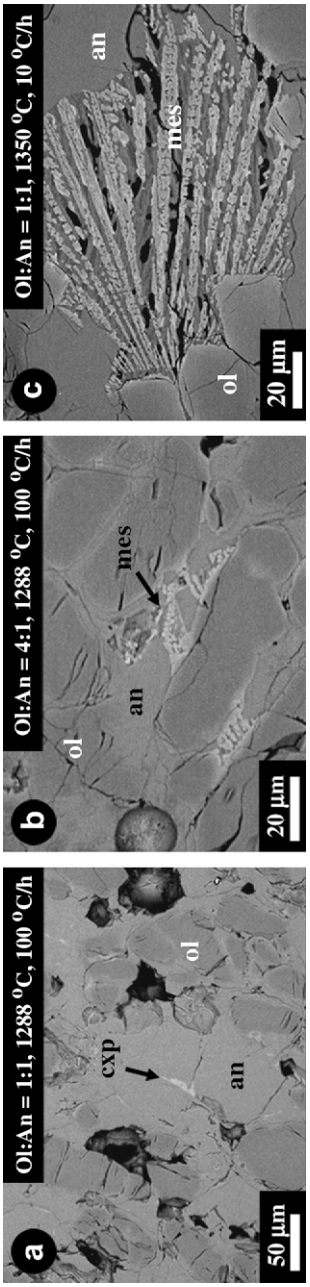

Fig. 6. Textural changes in olivine + anorthite mixtures with increasing heating temperature (cooling experiments) under the oxygen fugacity of IW. High-Ca pyroxene and mesostasis are present in the heated charges. The amount of high-Ca pyroxene and mesostasis is smaller in the charge heated at 1288 °C (a, b) than in the charge heated at 1350 °C (c). mes: Mesostasis.

pyroxene glass in each sample shows a wide range in composition (SiO_2: 43–46 wt%, Al_2O_3: 9–20 wt%, MgO: 9–18 wt%, CaO: 11–15 wt%). No systematic change in the abundance of high-Ca pyroxene glass is observed with varying proportion of olivine to anorthite (Table 8).

3.3.1.3. Olivine:anorthite = 1:1, heated at 1288 °C under the oxygen fugacity of QFM. We found no significant difference in composition between the samples heated under QFM and IW conditions. The QFM sample shows a wide range in concentrations of Al_2O_3, FeO, and MgO. To illustrate the range in chemical compositions, Table 9 lists individual analysis data for glass phases.

3.3.1.4. Forsterite:anorthite = 1:1, heated under the oxygen fugacity of IW. Table 9 lists the chemical compositions of forsterite + anorthite mixtures heated under the oxygen fugacity of IW. The high-Ca pyroxene glass, which is present in the samples heated at temperatures of 1308 °C–1318 °C, shows a wide range in Al_2O_3 (15–25 wt%) and MgO (13–18 wt%) concentrations (average compositions are listed in Table 10), as also found in charges comprising olivine + anorthite mixtures (10–20 wt% Al_2O_3, 11–30 wt% MgO).

3.3.2. Cooling experiments

Similar to quenched charges produced from isothermal experiments, forsterite and anorthite in charges after heating show no compositional changes, indicating that they did not melt or that they crystallized from the melt. High-Ca pyroxene in charges subjected to cooling experiments shows variable chemical composition (Table 11), especially in terms of Al_2O_3 and MgO content. No clear relationship was observed between composition and cooling rate. The compositional range of cooled charges is smaller than that of isothermal charges.

We also performed heating experiments on mixtures comprising forsterite, anorthite, and a small amount of perovskite. The high-Ca pyroxene in the perovskite-bearing charges shows a smaller compositional range than that in the charges comprising forsterite and anorthite mixtures. High-Ca pyroxene in the charges with 1 wt% perovskite (in the starting material) contains 0–8 wt% TiO_2 (Table 12), and its chemical composition overlaps with that of Al-diopside in AOAs. In our cooling experiments, no anorthite crystallized in charges heated above 1335 °C: only melt with the composition of anorthite + MgO is present (Table 13).

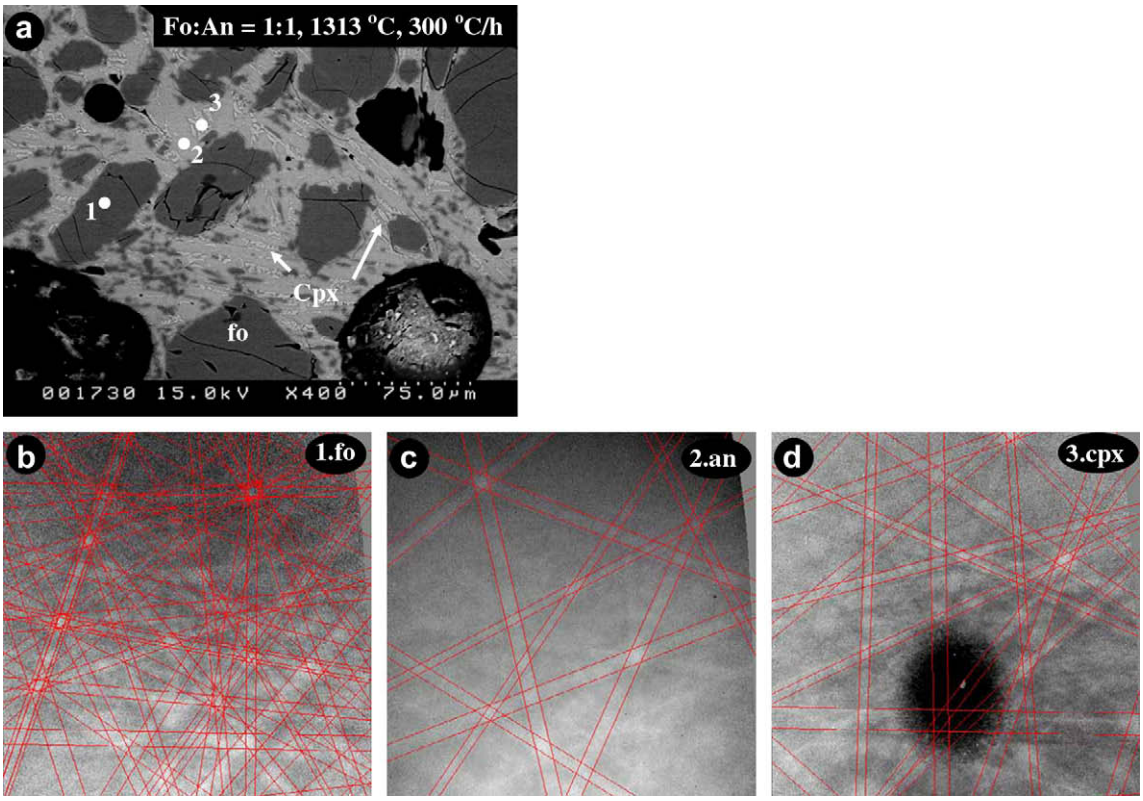

Fig. 7. (a) BSE image of a sample subjected to a cooling experiment (fo:an = 1:1, 1313 °C, cooling rate of 300 °C/h). Measurement spots are numbered 1–3. The EBSD patterns obtained for points #1 and #2 are indexed by the (b) forsterite and (c) anorthite crystal structures, respectively. Similarly, the obtained EBSD pattern of point #3 can be indexed by the (d) crystal structure of high-Ca pyroxene (space group *C2/c* structure).

4. Discussion

4.1. Evidence for high-temperature nebular processing of AOAs

4.1.1. Conflict with the equilibrium condensation model

Our study of AOAs from reduced CV chondrites that escaped secondary alteration reveals that primary refractory inclusions have a core–rim structure, with a core of spinel ± Al,Ti-rich diopside ± perovskite, an inner rim of anorthite, and an outer rim of Al-diopside. This finding suggests that the textures of AOAs cannot be produced by a simple condensation process. If AOAs originated as condensate assemblages, as proposed by Grossman and Steele (1976), their textures pose a problem. The observation that anorthite is rimmed by Al-diopside, which in turn is rimmed by olivine grains (considered to have originally been forsterite), is inconsistent with equilibrium condensation calculations that predict forsterite to condense prior to anorthite (e.g., Petaev and Wood, 2005). The condensation order is controlled by the total pressure (Ebel, 2006); however, these studies reported no differences in the condensation order of melilite, spinel, high-Ca pyroxene, and olivine. If anorthite in AOAs is not a condensation product, but instead a secondary mineral that replaced primary melilite (as suggested by Hashimoto and Grossman, 1987), this would also run counter to the observation that spinel is rimmed by anorthite. The mineralogy of AOAs implies that spinel formed before melilite, which is inconsistent with equilibrium condensation calculations that predict melilite should condense prior to spinel from a gas of solar composition.

4.1.2. Condensation of refractory minerals and forsterite

Table 14 compares the condensation sequences of gas with a solar composition, as variously calculated by Petaev and Wood (2005), Ebel and Grossman (2000), Yoneda and Grossman (1995), and Wood and Hashimoto (1993). Although there exist discrepancies in the condensation temperatures of Ca,Al-bearing

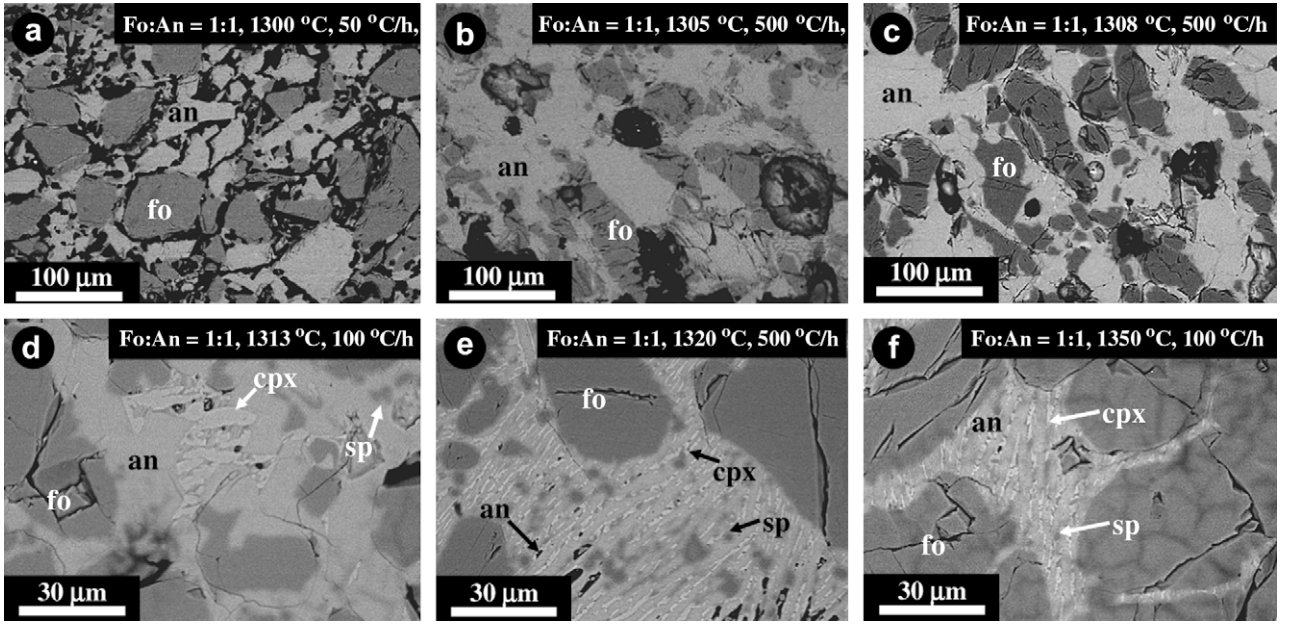

Fig. 8. Textural changes in mixtures of synthetic forsterite (Fo_{100}) and anorthite ($An_{95}Ab_5$) (fo:an = 1:1) with increasing heating temperature (cooling experiments) under the oxygen fugacity of IW. Anorthite and forsterite start melting at grain boundaries at 1305 °C (a, b). A small amount of high-Ca pyroxene is observed at 1308 °C (c). Abundant high-Ca pyroxene is results of isothermal and cooling experiments on olivine, forsterite + anorthite, and olivine + anorthite mixtures, and a mineralogical study of AOAs, we conclude that Al-diopside may have formed by the incipient melting of forsterite and anorthite observed in the charges heated at 1313 °C, occurring along anorthite grain boundaries (d) and occasionally surrounding forsterite. A number of lath-shaped anorthite crystals are observed in the charges heated at 1320 °C (e). Anorthite is completely melted at temperatures above 1337 °C, for which many lath-shaped anorthite crystals and high-Ca pyroxene crystals are observed (f). fo: forsterite, an: anorthite, cpx: high-Ca pyroxene, sp: spinel.

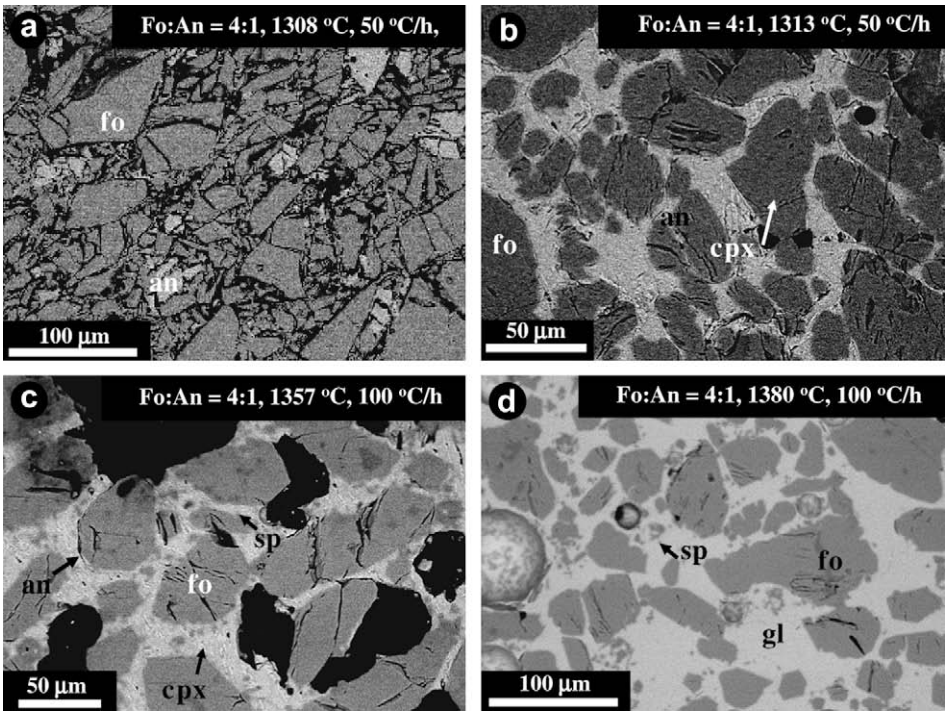

Fig. 9. Textural changes in mixtures of forsterite and anorthite with increasing heating temperature (cooling experiments). The textural changes observed in forsterite:anorthite = 4:1 charges with increasing heating temperature are similar to those observed in forsterite:anorthite = 1:1 charges, although less high-Ca pyroxene is produced in the former compared with the latter. fo: forsterite, an: anorthite, cpx: high-Ca pyroxene, sp: spinel.

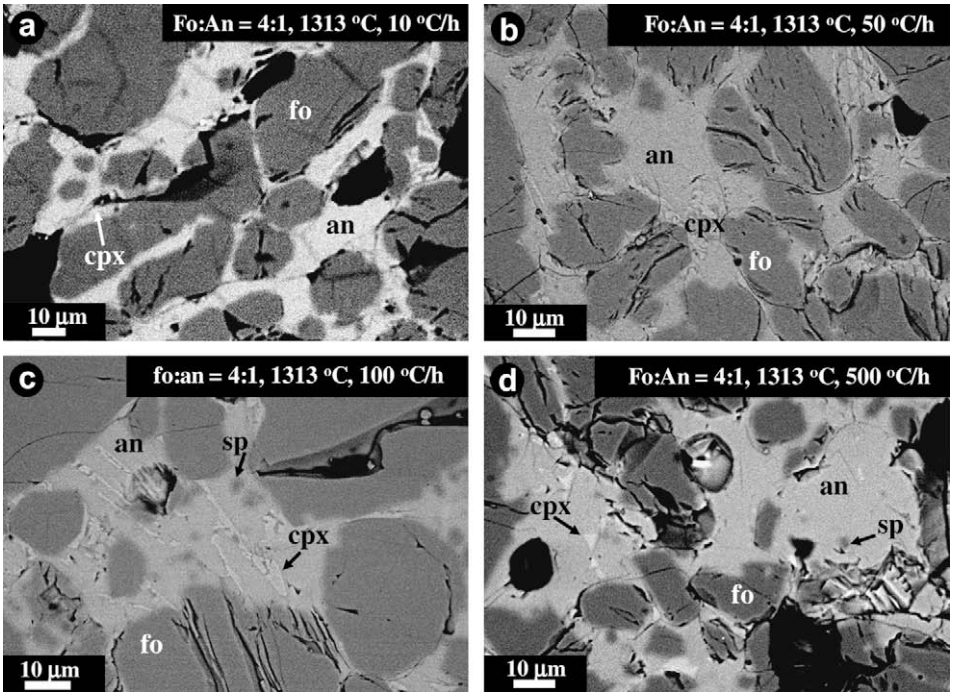

Fig. 10. Forsterite + anorthite mixtures cooled at various cooling rates. The charges heated at 1313 °C with a slow cooling rate (e.g., 10 °C/h) (a) contain less high-Ca pyroxene than those heated above 1313 °C with fast cooling rates (e.g., 500 °C/h) (d). fo: forsterite, an: anorthite, cpx: high-Ca pyroxene, sp: spinel.

Table 5
Average composition of high-Ca pyroxene glass.

	1288 °C	1337 °C	1438 °C
SiO_2	44.6	43.8	42.7
Al_2O_3	18.3	22.4	19.6
TiO_2	0.02	0.02	0.01
FeO	6.63	4.23	4.32
MnO	0.11	0.05	0.04
MgO	18.9	16.5	21.8
CaO	11.0	12.8	10.9
Na_2O	0.23	0.33	0.14
K_2O	0.01	0.00	0.01
Cr_2O_3	0.03	0.02	0.02
V_2O_3	0.01	0.03	0.01
NiO	0.12	0.11	0.09
Total	100.0	100.4	99.6
$Si/6O_x$	1.60	1.55	1.53
$Al/6O_x$	0.77	0.93	0.82
$Ti/6O_x$	0.00	0.00	0.00
$Fe/6O_x$	0.20	0.13	0.13
$Mn/6O_x$	0.00	0.00	0.00
$Mg/6O_x$	1.01	0.87	1.16
$Ca/6O_x$	0.42	0.49	0.42
$Na/6O_x$	0.02	0.02	0.01
$K/6O_x$	0.00	0.00	0.00
$Cr/6O_x$	0.00	0.00	0.00
Total	4.02	3.99	4.07

compounds, the condensation sequence of the constituent minerals within AOAs is similar among the different studies. Based on these equilibrium condensation calculations (e.g., Petaev and Wood, 2005), gehlenite is the first phase to appear, followed by spinel, metal, diopside, forsterite, and finally anorthite. The observation that spinel and melilite form a core shows that they condensed at higher temperatures than did the other minerals. Al,Ti-diopside is present with spinel in core regions, whereas Al-diopside forms rims around anorthite.

Table 6
Comparison of mineral compositions for heating durations of 3 and 100 h.

	3 h			100 h		
	Olivine	Anorthite	High-Ca pyroxene glass	Olivine	Anorthite	High-Ca pyroxene glass
SiO_2	40.6	44.2	44.6	41.3	44.3	45.1
Al_2O_3	0.30	35.8	18.3	0.05	35.3	18.7
TiO_2	0.01	0.02	0.02	0.01	0.02	0.03
FeO	7.46	0.52	6.63	5.23	0.29	3.88
MnO	0.09	0.01	0.11	0.11	0.03	0.10
MgO	50.0	0.12	18.9	51.7	0.77	22.6
CaO	0.22	19.4	11.0	0.21	18.9	9.34
Na_2O	0.01	0.27	0.23	0.00	0.06	0.02
K_2O	0.01	0.00	0.01	0.01	0.01	0.01
Cr_2O_3	0.02	0.01	0.03	0.03	0.02	0.03
V_2O_3	0.02	0.01	0.01	0.02	0.01	0.02
NiO	0.41	0.01	0.12	0.28	0.03	0.09
Total	99.1	100.4	100.0	99.0	99.7	100.0

This study reveals that AOAs have two occurrences of Al-diopside. We suggest that Al,Ti-diopside that occurs in cores is a primary condensate, whereas Al-diopside that occurs between anorthite and forsterite was produced by a reaction between anorthite and forsterite at high temperatures. According to equilibrium calculations, at a total pressure of $P = 10^{-3}$ atm, diopside condenses at 920 °C (Petaev and Wood, 2005), 912 °C (Ebel and Grossman, 2000), 903 °C (Yoneda and Grossman, 1995), or 871 °C (Wood and Hashimoto, 1993), after the condensation of spinel. It should be noted that the latter two condensation temperatures in the above list are based on Al-diopside, which may differ from the condensation temperature of Ti-bearing Al-diopside.

Petaev and Wood (2005) showed that the condensation temperature of Al,Ti-diopside is 17 °C higher than that of Al-diopside, as calculated by Yoneda and Grossman (1995) in a similar system. Therefore, it is likely that Al,Ti-diopside has a higher condensation temperature than does Al-diopside. The condensation of forsterite follows the condensation of diopside, and anorthite is the last phase to appear in the condensation sequence; however, anorthite forms within forsterite aggregates. This finding can be explained by the contrasting formation processes of forsterite and anorthite: forsterite condenses directly from solar gas, whereas anorthite forms by the reaction of spinel, diopside, and solar gas. Because anorthite is a precursor material at the temperature of forsterite condensation, the formation of anorthite is possibly faster than the condensation and aggregation of forsterite, thereby resulting in the following concentric texture: spinel + Al,Ti-diopside → anorthite → forsterite.

Condensation calculations predict forsterite to condense at a higher temperature than does anorthite. The difference in appearance temperature between forsterite and anorthite has been calculated to be 17 °C (Petaev and Wood, 2005), 14 °C (Ebel and Grossman, 2000), 27 °C (Yoneda and Grossman, 1995), and 60 °C (Wood and Hashimoto, 1993) at a total pressure of $P = 10^{-3}$ atm (Table 14). The concentric texture of AOAs can be explained as equilibrium condensation if the temperature interval between forsterite and anorthite condensation is small, as suggested in the models by Petaev and Wood (2005), Ebel and Grossman

Table 7
Comparison of the chemical composition of high-Ca pyroxene within experimental samples with varying olivine:anorthite ratios, subjected to heating at 1288 °C for 3 h under the oxygen fugacity of IW.

ol:an	9:1	4:1	7:3	3:1
SiO_2	46.4	41.3	40.1	43.7
Al_2O_3	20.0	9.32	11.0	20.1
TiO_2	0.03	0.01	0.00	0.02
FeO	6.57	6.92	6.40	4.86
MnO	0.15	0.10	0.09	0.09
MgO	11.9	36.4	37.8	21.2
CaO	13.5	4.77	4.59	10.2
Na_2O	0.16	0.10	0.10	0.29
K_2O	0.02	0.01	0.01	0.01
Cr_2O_3	0.01	0.04	0.03	0.05
V_2O_3	0.00	0.01	0.03	0.02
NiO	0.05	0.28	0.32	0.20
Total	98.7	99.3	100.5	100.7

(2000), and Yoneda and Grossman (1995). If the temperature interval is large as suggested in the model by Wood and Hashimoto (1993), the concentric texture of AOAs supports the idea that the phases formed under local disequilibrium condensation (Petaev et al., 2005).

4.1.3. High-temperature condensation reactions

Krot et al. (2004b) noted that the mineral assemblages observed in AOAs are inconsistent with the concept of equilibrium condensation, which predicts the disappearance of melilite before the condensation of forsterite. The authors explained that AOAs were originally condensates of melilite, spinel, and Al-diopside by the time of forsterite condensation, and that melilite reacted with gaseous Mg and SiO and was replaced by a fine-grained mixture of spinel, Al-diopside, and anorthite.

The relevant reactions are as follows. At the earliest stages of melilite alteration, the assemblage of melilite and spinel is replaced by Al-poor diopside:

Table 8
Modal abundances (ol:an:cpx) after heating at 1288 °C (IW) for various initial ol:an ratios, and various heating durations for ol:an = 1:1.

Original ratio	ol:an = 9:1	ol:an = 4:1	ol:an = 7:3	ol:an = 3:2
After heating				
Ol	83.2	65.2	65.3	51.8
An	65.2	22.9	38.3	38.3
Cpx	16.8	12.3	11.8	9.9
ol:an = 1:1				
(vol.%)	3 h	15 h	50 h	100 h
Ol	54.3	45.5	54.9	50.1
An	34.7	40.7	15.9	22.4
Cpx	11.0	13.7	29.1	27.5

$$3Ca_2Al_2SiO_{7(s)} + MgAl_2O_{4(s)} + 5SiO_{(g)} + Mg_{(g)} + 6H_2O \rightarrow [4CaAl_2SiO_6 + 2CaMgSi_2O_6]_{(px\ ss)} + 6H_{2(g)}. \quad (1)$$

Next,

$$Ca_2Al_2SiO_{7(s)} + 3SiO_{(g)} + Mg_{(g)} + 4H_2O \rightarrow CaAl_2SiO_{8(s)} + CaMgSi_2O_{6(s)} + 4H_{2(g)}. \quad (2)$$

Soon after, melilite is directly replaced by a mixture of diopside and spinel:

$$Ca_2Al_2SiO_{7(s)} + 3SiO_{(g)} + 3Mg_{(g)} + 6H_2O \rightarrow 2CaMgSi_2O_6 + MgAl_2O_{4(s)} + 6H_{2(g)}. \quad (3)$$

Al-diopside is much more abundant than melilite. We suggest that in addition to the reactions listed above, a reaction occurs between olivine and anorthite to produce Al-diopside.

4.1.4. Possible heating and partial melting of AOAs

Based on the following observations, we infer that AOAs may have experienced heating and incipient melting (Komatsu et al., 2001).

(i) Olivine triple-junction grain boundaries (Fig. 1c) and ‘‘doughnut-shaped’’ forsterite surrounding refractory inclusions (Fig. 1d) are relatively common features of AOAs, as described by Kornacki and Wood (1984a) and Bar-Matthews et al. (1979). Although little Fe,Ni-metal is found, spherical Fe,Ni-metal is occasionally observed (Fig. 1e). A plausible explanation of these textures is the heating and small degree of melting of AOAs.

(ii) Two types of Al-diopside (Al-diopside and Al,Ti-diopside; Fig. 1e) are present in AOAs, with different modes of occurrence. Al-diopside (generally 0–17 wt% Al_2O_3 and <3 wt% TiO_2) occurs between anorthite and forsterite, whereas Al,Ti-rich diopside (generally 20–30 wt% Al_2O_3 and 7–10 wt% TiO_2) is associated with spinel. Compositional variation in Al-diopside is difficult to explain by a simple condensation model, because Al must have already condensed by the time of condensation of gehlenite and spinel. Although we lack sufficient evidence to explain

Table 9
Average compositions of the constituent phases in the olivine:anorthite = 1:1 charge heated at 1288 °C, QFM[a].

	Olivine	Anorthite	Glass
SiO_2	41.0	43.8	44.6
Al_2O_3	0.04	35.4	34.6
TiO_2	0.01	0.01	0.02
FeO	6.52	0.41	3.50
MnO	0.10	0.01	0.07
MgO	52.2	0.42	20.6
CaO	0.34	19.5	16.5
Na_2O	0.00	0.32	0.41
K_2O	0.00	0.01	0.01
Cr_2O_3	0.00	0.00	0.03
V_2O_3	0.01	0.00	0.02
NiO	0.42	0.01	0.05
Total	100.6	99.9	99.8

[a] QFM = Quartz–Fayalite–Magnetite buffer.

why Al-diopside shows such a wide range in Al_2O_3 content, it may reflect the partial melting of forsterite and anorthite, as demonstrated by our heating experiments.

If a heating episode had occurred, there exist three possible sites for this event: (a) in the CAI-forming regions, (b) close to chondrule-forming regions, and (c) on a chondrite parent body. The results of heating experiments reveal that the anorthite + forsterite reaction occurs at temperatures above 1310 °C. Although heating of the parent body at this temperature would result in large-scale melting of the matrix and chondrules, there exists no evidence of such melting in CV chondrites; thus, the heating episode did not occur on the parent body. In addition, because thermal effects on the parent body were limited to alteration at relatively low temperatures of <500 °C (e.g., Krot et al., 1995), the heating episode can be considered separately from alteration of the parent body.

Table 10
Average compositions of high-Ca pyroxene glass in the forsterite:anorthite = 1:1 charges.

	1303 °C	1313 °C	1318 °C
SiO_2	46.6	47.9	47.1
Al_2O_3	22.9	18.8	21.7
TiO_2	0.07	0.06	0.02
FeO	0.35	0.41	0.16
MnO	0.00	0.01	0.02
MgO	13.6	17.8	15.0
CaO	15.5	14.7	15.2
Na_2O	0.36	0.39	0.11
K_2O	0.02	0.02	0.01
Cr_2O_3	0.02	0.02	0.02
V_2O_3	0.02	0.03	0.02
NiO	0.02	0.02	0.01
Total	99.5	100.1	99.4

In the case that the heating episode took place in the CAI-forming region, the best estimate of cooling in this region, as obtained from type B CAIs, is approximately 1–10 °C/h (Stolper and Paque, 1986). In contrast, if the heating episode took place in the chondrule-forming regions, the phases would have cooled at a rate of approximately 5–2000 °C/h (e.g., Hewins, 1996). The presence of crystalline Al-diopside in AOAs indicates relatively slow cooling. Based on these calculations, both the chondrule-forming and CAI-forming regions are potential sites of annealing; however, heating in the CAI-forming regions is favored by the fact that oxygen and magnesium isotope measurements of AOAs from primitive chondrites (Krot et al., 2004d) indicate that the vast majority of AOAs formed in the CAI-forming regions. The incomplete melting of olivine and anorthite indicates a heating period of limited duration.

4.2. Characteristics of high-Ca pyroxenes in AOAs and heated samples

4.2.1. Bulk composition of AOAs: petrogenetic link to olivine and anorthite

On a Al_2O_3–Mg_2SiO_4–Ca_2SiO_4 ternary diagram, the bulk compositions of AOAs from reduced CV chondrites (Komatsu et al., 2001) plot along a line extending from forsterite toward anorthite and melilite (Fig. 11), consistent with the known mineralogy of AOAs. The data mainly plot along the mixing line between forsterite and anorthite, indicating a genetic relationship between these minerals and AOAs. In addition, the bulk compositions of AOAs do not plot along the trend of bulk condensed solid for the equilibrium condensation sequence proposed by Yoneda and Grossman (1995). MacPherson and Huss (2000) suggested that differences between the bulk composition of CAIs and chondrules, and the calculated trend for bulk condensed solids during equilibrium condensation reflect the complicated nature of the condensation and evaporation process; however, it is unlikely that AOAs have experienced extensive melting and evaporation.

4.2.2. Reaction of olivine and anorthite

We found slight changes in melting temperature of anorthite and olivine depending on the olivine:anorthite ratio in the starting material and oxygen fugacity.

Table 11
Average compositions of high-Ca pyroxenes from the results of cooling experiments of forsterite and anorthite.

fo:an	1:1	1:1	1:1	1:1	1:1	4:1	4:1		4:1	4:1	4:1
T	1313 °C	1313 °C	1313 °C	1320 °C	1320 °C	1313 °C	1313 °C		1313 °C	1320 °C	1320 °C
C.R	10 °C/h	50 °C/h	300 °C/h	10 °C/h	500 °C/h	10 °C/h	50 °C/h		300 °C/h	10 °C/h	500 °C/h
No.	4	26	29	4	11	1	17		13	1	7
	cpx	cpx	cpx	cpx	cpx	cpx	sp	cpx	cpx	cpx	cpx
SiO_2	45.2	50.9	46.3	54.0	45.5	44.1	1.8	51.0	46.3	43.7	48.3
Al_2O_3	26.9	13.6	20.4	9.84	20.1	24.6	72.0	14.1	19.4	29.2	20.3
TiO_2	0.00	0.05	0.02	0.07	0.02	0.00	0.02	0.06	0.01	0.00	0.01
FeO	0.17	0.24	0.36	0.63	0.60	0.27	0.18	0.15	0.15	0.03	0.16
MnO	0.01	0.03	0.02	0.03	0.02	0.00	0.01	0.03	0.02	0.00	0.00
MgO	18.3	15.9	19.0	18.4	19.7	18.9	26.9	15.0	19.4	14.1	13.6
CaO	12.7	18.8	14.4	17.2	13.6	13.5	0.6	18.8	14.5	14.5	17.3
Na_2O	0.23	0.25	0.29	0.24	0.25	0.15	0.01	0.34	0.19	0.28	0.35
K_2O	0.01	0.03	0.02	0.03	0.01	0.01	0.00	0.05	0.01	0.00	0.01
Cr_2O_3	0.02	0.01	0.01	0.00	0.02	0.04	0.00	0.01	0.02	0.00	0.01
V_2O_3	0.03	0.01	0.01	0.01	0.04	0.06	0.00	0.01	0.02	0.00	0.01
NiO	0.01	0.01	0.00	0.02	0.02	0.01	0.00	0.01	0.01	0.00	0.01
Total	103.5	99.8	100.9	100.5	99.9	101.7	101.5	99.6	100.0	101.9	100.1
$Na/6O_x$	0.01	0.02	0.02	0.02	0.02	0.01		0.02	0.0	0.02	0.02
$Mg/6O_x$	0.92	0.83	0.98	0.96	1.03	0.97		0.79	1.0	0.72	0.71
$Al/6O_x$	1.05	0.56	0.83	0.40	0.83	1.00		0.59	0.8	1.17	0.83
$Si/6O_x$	1.51	1.80	1.60	1.88	1.59	1.51		1.80	1.6	1.49	1.69
$K/6O_x$	0.00	0.00	0.00	0.00	0.00	0.00		0.00	0.0	0.00	0.00
$Ca/6O_x$	0.46	0.71	0.53	0.65	0.51	0.50		0.71	0.5	0.53	0.65
$Ti/6O_x$	0.00	0.00	0.00	0.00	0.00	0.00		0.00	0.0	0.00	0.00
$Cr/6O_x$	0.00	0.00	0.00	0.00	0.00	0.00		0.00	0.0	0.00	0.00
$Mn/6O_x$	0.00	0.00	0.00	0.00	0.00	0.00		0.00	0.0	0.00	0.00
$Fe/6O_x$	0.00	0.01	0.01	0.02	0.02	0.01		0.00	0.0	0.00	0.00
$cats/6O_x$	3.97	3.93	3.99	3.92	4.00	3.99		3.92	4.0	3.93	3.91
Wo	34.0	47.3	35.6	40.1	34.9	33.8		48.7	35.4	42.5	48.0
Fs	0.3	0.4	63.8	0.7	1.1	1.1		0.5	0.3	0.1	0.4

Isothermal experiments on olivine + anorthite heated under the oxygen fugacity of IW revealed that a high-Ca pyroxene glass was produced from the reaction of olivine and anorthite when heated at 1288 °C. The experimental findings of the overgrowth of high-Ca pyroxene glass on olivine and the sharp boundary between the glass and anorthite are consistent with the occurrence of Al-diopside in natural AOAs (Fig. 2d). Heating experiments were performed mainly under the oxygen fugacity of IW. Although it is generally believed that CAIs and AOAs formed under reducing condition below the IW buffer (Dyl et al., 2005; Krot et al., 2000), slightly more oxidizing conditions were chosen to avoid any significant evaporation of silicon and magnesium. In addition, strongly reducing conditions (e.g., those of IW-2) are difficult to achieve by the mixing of CO_2 and H_2 gas. We found no significant difference in the results obtained using IW and QFM buffers.

Given that the bulk composition of natural AOAs is similar to that of the olivine:anorthite = 4:1 sample, it is likely that the textural changes observed in this latter sample are comparable to the reaction recorded by AOAs (Table 4). The high-Ca pyroxene glass occurs at 1288 °C via a reaction between olivine and anorthite (Fig. 4); thereafter, its abundance increases with increasing heating temperature until anorthite is completely melted in the sample heated at 1293 °C. Similar textural changes are observed in the samples with olivine:anorthite ratios between 1:1 and 9:1, producing similar textures to those observed in AOAs (Fig. 3). It is likely that Al-diopside in AOAs formed from a starting material with a wide range of olivine:anorthite ratios.

The present isothermal experiments reveal that high-Ca pyroxene glass is 2–10 μm in size in the <37 μm ol + an sample, and 5–20 μm in the <100 μm sample. Larger high-Ca pyroxene glasses were formed in experiments with coarser starting materials. The results of cooling experiments reveal that the grain size of high-Ca pyroxene increases with decreasing cooling

Table 12
Average compositions of high-Ca pyroxene in perovskite (Pv)-bearing charges[a]

fo:an	1:1 + Pv1 wt%	1:1 + Pv 5 wt%	4:1 + Pv 5 wt%	
T	1320 °C	1308 °C	1308 °C	
	cpx	cpx	sp	cpx
SiO_2	45.3	44.2	2.7	43.2
Al_2O_3	17.6	8.85	63.6	13.1
TiO_2	2.46	7.66	0.93	7.54
FeO	0.29	1.27	0.12	0.63
MnO	0.01	0.01	0.00	0.01
MgO	17.2	17.5	26.4	14.7
CaO	16.1	21.2	0.9	20.0
Na_2O	0.27	0.28	0.04	0.30
K_2O	0.02	0.00	0.01	0.01
Cr_2O_3	0.04	0.06	0.03	0.04
V_2O_3	0.02	0.06	0.00	0.06
NiO	0.00	0.00	0.00	0.00
Total	99.2	101.0	94.7	99.6
$Na/6O_x$	0.02	0.02		0.02
$Mg/6O_x$	0.91	0.94		0.79
$Al/6O_x$	0.74	0.38		0.56
$Si/6O_x$	1.61	1.60		1.57
$K/6O_x$	0.00	0.00		0.00
$Ca/6O_x$	0.61	0.82		0.78
$Ti/6O_x$	0.07	0.21		0.21
$Cr/6O_x$	0.00	0.00		0.00
$Mn/6O_x$	0.00	0.00		0.00
$Fe/6O_x$	0.01	0.04		0.02
$cats/6O_x$	3.97	4.01		3.95
Wo	40.0	45.8		49.8
Fs	0.6	2.1		1.1

[a] All samples were cooled at a rate of 500 °C/h.

rate, although never exceeding the original grain size. Based on the observation that high-Ca pyroxene in AOAs is <10 μm in size, we estimate that the original grain sizes of olivine and anorthite were probably less than 37 μm. We observed systematic changes in the MgO content of high-Ca pyroxene glass in isothermal experiments, reflecting increasing melting of olivine with increasing temperature (Table 5).

Rapid-cooling experiments on olivine + anorthite reveal the formation of mesostasis that contains lath-like high-Ca pyroxene. Because no such mesostasis is observed in AOAs, it is likely that the experimental cooling rate was higher than that experienced by AOAs.

4.2.3. Reaction of forsterite and anorthite

In the cooling experiments, high-Ca pyroxene was observed in the samples subjected to temperatures of 1308 °C–1320 °C, resulting from the incomplete melting of forsterite and anorthite. High-Ca pyroxene was also observed to result from a reaction between forsterite and highly melted anorthite at temperatures up to 1350 °C (Figs. 8 and 9). At temperatures above 1350 °C, however, anorthite is completely melted and only a small number of tiny grains of high-Ca pyroxene are observed (Fig. 9d). It appears that the slowly cooled charges contain slightly fewer high-Ca pyroxenes than do the rapidly cooled charges. The grain size of high-Ca pyroxene is larger in the slowly cooled charges than in the rapidly cooled charges, in which lath-shaped anorthite and high-Ca pyroxene are commonly observed. This finding is consistent with a previous experimental study of chondrules (Radomsky and Hewins, 1990) that reported a change from barred to porphyritic texture with decreasing cooling rate.

Based on a series of dynamic crystallization experiments, Radomsky and Hewins (1990) noted that the abundance of nuclei is a primary factor in controlling textural development, whereas cooling rate plays a secondary role. In the present study, no anorthite crystallized from melt in charges heated at temperatures above 1350 °C and with cooling rates of 10–500 °C/h, probably because few nuclei of anorthite remained in the melt. If the charges had been cooled more slowly, anorthite might well have recrystallized from the melt (Radomsky and Hewins, 1990).

Table 13
Chemical compositions of high-Ca pyroxenes in heated samples and AOAs.

wt %	Run products, isothermal		Run products, cooled			AOA	
	ol + an	fo + an	fo + an	fo + an + pv 1%	fo + an + pv 5%	Al-diopside	Al,Ti-diopside
SiO_2	40–45	43–48	43–54	40–47	36–45	48–53	36–38
Al_2O_3	10–20	15–25	7–23	8–20	13–19	0–17	20–30
TiO_2	0	0	0	0–8	1–12	0–3	7–10
FeO	6–7	0	0	0	0	0–1	0–1
MgO	11–30	13–18	11–24	15–20	10–18	14–16	9–10
CaO	5–16	15–17	14–20	19–22	15–23	17–25	25

Table 14
Comparison of condensation temperatures (°C) from different condensation calculations.

Mineral	Petaev and Wood (2005) CWPI[a]		Ebel and Grossman (2000)		Yoneda and Grossman (1995)		Wood and Hashimoto (1993)	
	In	Out	In	Out	In	Out	In	Out
Corundum, Al_2O_3	1502	1478	1497	1453	1497	1467	1490	1484
Hibonite, $CaAl_4O_7$	1497	1222	1455	1413	1470	1227	1480	1259
Grossite, $CaAl_{12}O_{19}$	1383	1333	1425	1321	–	–	1259	1243
Perovskite, $CaTiO_3$	1419	1192	1407	1185	1415	1175		
$CaAl_2O_4$	–	–	1351	1295	–	–		
Melilite ss.	1335	1177	1307	1161	1352	1171	1382	1144
Grossite	–	–	1295	1229	–	–		
Hibonite	–	–	1229	1215	–	–		
Spinel ss.	1222	1158	1215	1127	1228	1136	1243	1125
Metal ss.	1199		1189		1191		Fe–Si 1187	
Cpx ss.	1193		1185		Fassaite 1176		Di–CaTs 1144	
Olivine ss.	1176		1171		Forsterite 1170		1187	
Plagioclase ss.	1187		1133	1045	1143		1127	
Ti_3O_5	1107	1009	1095	1069	1113	1088		
Orthopyroxene ss.	1099		1093		1093			

[a] CWPI is based on condensation with partial isolation model.

4.2.4. Compositional variations in high-Ca pyroxene

The compositions of high-Ca pyroxene (including glass) in the olivine + anorthite and forsterite + anorthite charges overlap with the compositions of Al-diopside in AOAs from CV chondrites (Table 13), although high-Ca pyroxene from the olivine + anorthite mixture has higher FeO concentrations (6–7 wt%) and lower CaO concentrations (5–16 wt%) than do AOAs (0–1 wt% FeO, 17–25 wt% CaO). The compositions of high-Ca pyroxene glasses in forsterite + anorthite charges subjected to isothermal experiments also overlap with those of AOA pyroxenes, and pyroxenes from both heated samples tend to have lower CaO concentrations (15–17 wt%) than do natural AOAs. Similar high-Ca pyroxene compositions were found between AOA and charges of forsterite + anorthite + 1 wt% perovskite (19–22 wt% CaO); therefore, we cannot exclude the possibility of Al-diopside formation via the heating of pre-existing forsterite and anorthite.

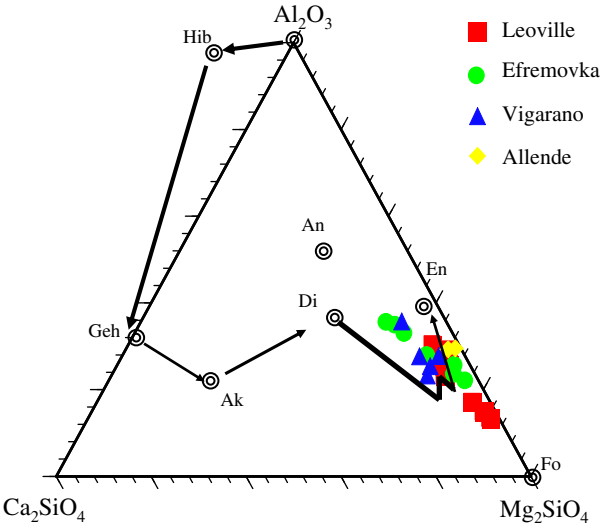

Fig. 11. Bulk compositions of AOAs from CV chondrites plotted in an Al_2O_3–Mg_2SiO_4–Ca_2SiO_4 ternary diagram. Also shown for comparison (arrows) is the calculated trajectory for bulk solids during the high-temperature equilibrium condensation of a solar composition gas (Yoneda and Grossman, 1995). Geh: gehlenite, Ak: akermanite, An: anorthite, Di: diopside, En: enstatite, Fo: forsterite.

4.2.5. Formation of high-Ca pyroxene by heating

The heating experiments involving olivine, forsterite, and anorthite indicate the occurrence of complex reactions in response to heating. The modal abundance of refractory minerals varies among the various AOAs. Some refractory nodules contain spinel + anorthite + Al-diopside, whereas others contain only Al-diopside. Differences in the modal abundance of anorthite and Al-diopside could be explained in terms of the degree of reaction associated with heating. Mineralogical observations indicate that smaller refractory nodules have simpler mineralogy (e.g., Al-diopside as a sole constituent), whereas larger refractory nodules have more complex mineralogy (e.g., Al-diopside, anorthite, and occasionally spinel). Our heating experiments revealed that melting is influenced by the olivine:anorthite ratio; consequently, the relationship between size and mineralogy can be explained in terms of the pre-existing condition before

melting: if anorthite grains are small, they are completely melted to form Al-diopside, whereas if anorthite grains are sufficiently large, only partial melting occurs.

Because the modal abundance of Al-diopside and spinel is much lower than that in natural AOAs, it is unlikely that all of the Al-diopside and spinel in AOAs formed by the reaction between olivine and anorthite, however, the results of the present heating experiments and EBSD analysis indicate that some Al-diopside and possibly some spinel may have formed by the incipient melting of forsterite and anorthite. The diopside-forming reaction is as follows (Fig. 12):

$$Mg_2SiO_4 + CaAl_2Si_2O_8 \rightarrow CaMgSi_2O_6 + MgAl_2O_4 + SiO_2 \quad (4)$$

Previous oxygen-isotopic studies of AOAs have reported that Al-diopside (and/or anorthite) in AOAs from CV3 chondrites yield smaller $\delta^{18}O$ values than does forsterite in the same AOAs (Fagan et al., 2002; Hiyagon and Hashimoto, 1999; Krot et al., 2002), suggesting that olivine and Al-diopside may have formed under slightly different environments. The difference in $\delta^{18}O$ values between forsterite and Al-diopside can be explained if the annealing event that affected AOAs and Al-diopside arose from the incomplete melting of forsterite and anorthite.

4.3. Removal of AOAs from CAI-forming regions

The solar nebula gas is inferred to have a Mg:Si ratio of ~1 (Anders and Grevesse, 1989). According to equilibrium condensation calculations, the condensation of forsterite (Mg:Si = 2) from a solar nebula gas at a total pressure of 10^{-5} bar at ~1047 °C is followed by the condensation of Fe,Ni-metal at ~1189 °C; enstatite (Mg:Si = 1) forms at ~1099 °C via a reaction between forsterite and residual Si-rich gas (Petaev and Wood, 2005). Kornacki and Wood (1984a,b) explained the complete absence of enstatite in AOAs from Allende in terms of highly oxidizing conditions during AOA formation, which resulted in the condensation of fayalitic olivine instead of low-Ca pyroxene; however, this hypothesis cannot explain the lack of enstatite in AOAs from reduced CV chondrites, which are characterized by Mg-rich olivine compositions. It is clear that the ferrous composition of olivine in Allende is the result of secondary alteration that postdates the condensation of AOA olivines (Krot et al., 2004c). Indeed, a previous oxygen-isotopic study of AOAs from Allende revealed that ^{16}O-rich forsterite is primitive and that ^{16}O-poor ferroan olivine formed during alteration within an environment with ^{16}O-poor isotopic compositions (Imai and Yurimoto, 2001).

Previous studies of primitive AOAs containing low-Ca pyroxenes (Krot et al., 2004d, 2005) indicate that AOAs are aggregates of solar nebular condensates that originated in an ^{16}O-rich gaseous reservoir(s), probably in CAI-forming regions. The depletion of AOAs in Fe,Ni-metal and moderately volatile elements (Mn, Na, and K) indicates that they were chemically isolated from hot nebular gas prior to the condensation of Fe,Ni-metal, enstatite or silica, and moderately volatile elements. This chemical isolation may have occurred via the physical removal of AOAs from a region rich in ^{16}O gas to a region poor in ^{16}O gas, where all the major rock-forming elements (Si, Mg, Fe, Ni, Mn, Na, K, and S) had already condensed (e.g., Shu et al., 2001).

4.4. Relation between AOAs and fine-grained spinel-rich inclusions

Fine-grained spinel-rich inclusions (FGIs) share common textural features with AOAs, indicating a genetic relationship (Lin and Kimura, 2003). As described in Section 4.2.2, one of the characteristics of refractory inclusions in AOAs is that spinel and Al,Ti-diopside are surrounded by anorthite. This core–rim texture of spinel + anorthite is also observed in FGIs.

The origin of FGIs remains under discussion (e.g., Krot et al., 2004b). MacPherson et al. (2002) described the detailed mineralogical characteristics of FGIs from Efremovka and Leoville. These authors demonstrated that zoning structures in FGIs (i.e., spinel-rich and melilite-absent cores, and melilite-rich mantles) are primary, not the result of the preferential alteration of melilite to form anorthite in inclusion cores. Krot et al. (2004c) proposed that FGIs originally formed as aggregates of spinel + perovskite + melilite ± hibonite gas–solid condensates. These aggregates later underwent low-temperature gas–solid nebular reactions with gaseous SiO and Mg to form Al-diopside ± anorthite (Krot et al., 2004c). It should be noted that anorthite in the cores was interpreted to be a replacement product from spinel, not an alteration product of melilite.

Aléon et al. (2002) reported that oxygen-isotopic data for mantle FGIs are indicative of mass-dependent isotopic fractionation, indicating late-stage partial melting accompanied by evaporation. If FGIs have indeed experienced such late-stage partial melting and evaporation, the question arises as to how this environment affected AOAs. Because previous

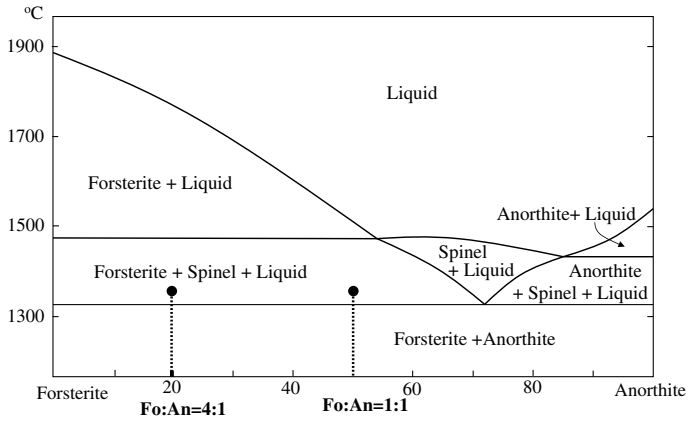

Fig. 12. Phase diagram of the forsterite–anorthite system (Osborn and Tait, 1952). The dashed lines show the compositions of the starting materials (fo:an = 1:1 and 4:1). Based on the results of isothermal and cooling experiments on olivine, forsterite + anorthite, and olivine - + anorthite mixtures, and a mineralogical study of AOAs, we conclude that Al-diopside may have formed by the incipient melting of forsterite and anorthite.

oxygen-isotopic studies have shown that AOAs and FGIs formed under similar environments (e.g., Fagan et al., 2002), it is likely that AOAs experienced the same reactions as did FGIs.

Although there are insufficient data to discuss the condensation origin of anorthite in AOAs, it probably represents a replacement product of spinel during an open-system reaction that occurred in the hot nebula. It should be noted that despite the fact that FGIs contain a large amount of spinel, the abundance of spinel in AOAs is limited (less than 15 vol.%). If the reaction suggested by MacPherson et al. (2002) actually occurred, the small amount of spinel in AOAs can be explained by the extensive replacement of spinel by anorthite. In any event, it is clear that FGIs and AOAs have more complex histories than previously thought (e.g., Kornacki and Wood, 1984a).

5. Conclusion

Mineralogical observations and heating experiments of the present study reveal that AOAs have a more complex thermal history than previously considered (e.g., Hashimoto and Grossman, 1987). It is suggested that AOAs represent aggregates of high-temperature nebular condensates that formed in CAI-forming regions, and that they were absent from chondrule-forming regions at the time of chondrule formation. It is also shown that AOAs experienced a heating event that resulted in the development of triple-junction grain boundaries in olivine and rounded shapes of Fe,Ni-metal, indicating the influence of a thermal event in either the CAI- or chondrule-forming regions. Small amounts of Al-diopside may have been produced by a small degree of melting of olivine, anorthite, and possibly previously condensed Al,Ti-diopside during the heating event.

Below, we list the sequence of events involved in the formation of AOAs, based on mineralogical observations and heating experiments (condensation temperatures for Al,Ti-diopside are based on Yoneda and Grossman, 1995 and Petaev and Wood, 2005).

1. Condensation of perovskite, melilite, and spinel followed by Al,Ti-diopside from the solar gas (∼1193 °C).
2. Replacement of melilite by spinel, Al-diopside, and anorthite.
3. Condensation of forsterite (∼1176 °C).
4. Formation of aggregates of the above minerals.
5. Physical removal of AOAs from hot condensation regions into cold regions.
6. After aggregation, some Al-diopside and spinel may have formed by the incomplete reaction (>1300 °C, as determined from heating experiments) of anorthite and forsterite.
7. Accretion of CV parent body.
8. Secondary alteration leading to the replacement of anorthite and melilite by nepheline and sodalite.

Acknowledgments

We thank the National Institute for Polar Research and Dr. A. Ulyanov for lending us thin sections for

analysis. We also thank Drs. T. Kogure and T. J. Fagan for useful discussions, and Mr. H. Yoshida and Mr. O. Tachikawa for technical assistance during electron beam analysis. We thank Drs. A. Yamaguchi, M. Kimura, and A. N. Krot for their helpful reviews, constructive comments, and assistance in improving the English in the manuscript. Electron microscopy was performed in the Electron Microbeam Analysis Facility for Mineralogy at the Department of Earth and Planetary Science, University of Tokyo. This work was supported by a Fellowship for Young Scientists (#15-10423) of the Japan Society for the Promotion of Science.

References

Aléon, J., Krot, A.N., McKeegan, K.D., MacPherson, G.J., Ulyanov, A.A., 2002. Oxygen isotopic composition of fine-grained Ca, Al-rich inclusions in the reduced CV3 chondrite Efremovka. Lunar Planet. Sci. 33 CD-ROM #1426.

Anders, E., Grevesse, N., 1989. Abundances of the elements − meteoritic and solar. Geochim. Cosmochim. Acta 53, 197−214.

Bar-Matthews, M., MacPherson, G.J., Grossman, L., 1979. An SEM−petrographic study of amoeboid olivine aggregates in Allende (abstract). Meteoritics 14, 342.

Brett, R., Sato, M., 1984. Intrinsic oxygen fugacity measurements on seven chondrites, a pallasite, and a tektite and the redox state of meteorite parent bodies. Geochim. Cosmochim. Acta 48, 111−120.

Chizmadia, L.J., Rubin, A.E., 2000. Petrology and origin of amoeboid olivine inclusions in CO3 chondrites (abstract). Lunar Planet. Sci. 31 CD-ROM #1494.

Cohen, R.E., Kornacki, A.L., Wood, J.A., 1983. Mineralogy and petrology of chondrites and inclusions in the Mokoia CV3 chondrite. Geochim. Cosmochim. Acta 47, 1739−1757.

Cuzzi, J.N., Zahnle, K.J., 2004. Material enhancement in protoplanetary nebulae by particle drift through evaporation fronts. Astrophys J 614, 490−496.

Dudarev, S.L., Rez, P., Whelan, M.J., 1995. Theory of electron backscattering from crystals. Phys Rev B 51, 3397−3412.

Dyl, K.A., Simon, J.I., Russel, S.S., Young, E.D., 2005. Rapidly changing oxygen fugacity in the early solar nebula recorded by CAI rims. Lunar Planet. Sci. 36 CD-ROM #1531.

Ebel, D.S., 2006. Condensation of rocky minerals in astrophysical environments. In: Lauretta, D.S., McSween, H.Y. (Eds.), Meteorites and the Early Solar System. The University of Arizona Press, Tuscon, pp. 253−277.

Ebel, D.S., Grossman, L., 2000. Condensation in dust-enriched systems. Geochim. Cosmochim. Acta 64, 339−366.

Fagan, T.J., Yurimoto, H., Krot, A.N., Keil, K., 2002. Similarities and differences in oxygen isotopic evolution of fine vs. coarse refractory inclusions in the reduced CV3 Efremovka. Meteorit. Planet. Sci. 39, 1517−1553.

Grossman, L., Steele, I.M., 1976. Amoeboid olivine aggregates in the Allende meteorite. Geochim. Cosmochim. Acta 40, 149−155.

Hashimoto, A., Grossman, L., 1987. Alteration of Al-rich inclusions inside amoeboid olivine aggregates in the Allende meteorite. Geochim. Cosmochim. Acta 51, 1685−1704.

Hewins, R.H., 1996. Chondrules and the protoplanetary disk: an overview. In: Hewins, R.H., Jones, R.H.E., Scott, E.R.D. (Eds.), Chondrules and the Protoplanetary Disk. Cambridge University Press, Cambridge, pp. 3−9.

Hiyagon, H., Hashimoto, A., 1999. 16O excesses in olivine inclusions in Yamato-86009 and Murchison chondrites and their relation to CAIs. Science 283, 828−831.

Imai, H., Yurimoto, H., 2001. Two generations of olivine-growth in an amoeboid olivine aggregate from the Allende meteorite. Lunar Planet. Sci. 32 CD-ROM #1580.

Kogure, T., 2003. A program to assist Kikuchi pattern analyses. J. Cryst. Soc. Jpn. 45, 391−395.

Komatsu, M., Krot, A.N., Petaev, M.I., Ulyanov, A.A., Keil, K., Miyamoto, M., 2001. Mineralogy and petrography of amoeboid olivine aggregates from the reduced CV3 chondrites Efremovka, Leoville and Vigarano: products of nebular condensation, accretion and annealing. Meteorit. Planet. Sci. 36, 629−641.

Kornacki, A.S., Wood, J.A., 1984a. Petrography and classification of Ca, Al-rich and olivine-rich inclusions in the Allende CV3 chondrite. J. Geophys. Res. 89, B573−B587.

Kornacki, A.S., Wood, J.A., 1984b. The mineral chemistry and origin of inclusion matrix and meteorite matrix in the Allende CV3 chondrite. Geochim. Cosmochim. Acta 48, 1663−1676.

Krot, A.N., Fegley Jr., B., Lodders, K., Palme, H., 2000. Meteoritical and astrophysical constraints on the oxidation state of the solar nebula. In: Mannings, V., Boss, A.P., Russel, S.S. (Eds.), Protostars and Planets IV. Univeristy of Arizona Press, Tucson, pp. 1019−1054.

Krot, A.N., McKeegan, K.D., Leshin, L.A., MacPherson, G.J., Scott, E.R.D., 2002. Existence of an 16O-rich gaseous reservoir in the solar nebula. Science 295, 1051−1054.

Krot, A.N., Petaev, M.I., Russel, S.S., Itoh, S., Fagan, T.J., Yurimoto, H., Chizmadia, L., Weisberg, M.K., Komatsu, M., Ulyanov, A.A., Keil, K., 2004a. Amoeboid olivine aggregates and related objects in carbonaceous chondrites: records of nebular and asteroid processes. Chemie der Erde 64, 185−239.

Krot, A.N., MacPherson, G.J., Ulyanov, A.A., Petaev, M.I., 2004b. Fine-grained, spinel-rich inclusions from the reduced CV chondrites Efremovka and Leoville: I. Mineralogy, petrology, and bulk chemistry. Meteorit. Planet. Sci. 39, 1517−1553.

Krot, A.N., Petaev, M.I., Bland, P.A., 2004c. Multiple formation mechanisms of ferrous olivine in CV carbonaceous chondrites during fluid-assisted metamorphism. Antarct. Meteorite Res. 17, 153−171.

Krot, A.N., Petaev, M.I., Yurimoto, H., 2004d. Amoeboid olivine aggregates with low-Ca pyroxenes: a genetic link between refractory inclusions and chondrules? Geochim. Cosmochim. Acta 68, 1923−1941.

Krot, A.N., Scott, E.R.D., Zolensky, M.E., 1995. Mineralogical and chemical modification of components in CV3 chondrites: nebular or asteroidal processing? Meteoritics 30, 748−775.

Krot, A.N., Fagan, T.J., Nagashima, K., Petaev, M.I., Yurimoto, H., 2005. Origin of low-Ca pyroxene in amoeboid olivine aggregates: evidence from oxygen isotopic compositions. Geochim. Cosmochim. Acta 69, 1873−1881.

Lin, Y., Kimura, M., 2003. Ca−Al-rich inclusions from the Ningqiang meteorite: continuous assemblages of nebular condensates and genetic link to Type B inclusions. Geochim. Cosmochim. Acta 67, 2251−2267.

MacPherson, G.J., Huss, G.R., 2000. Convergent evolution of cais and chondrules: evidence from bulk compositions and a cosmochemical phase diagram. Lunar Planet. Sci. 31 CD-ROM #1796.

MacPherson, G.J., Krot, A.N., Ulyanov, A.A., Hicks, T., 2002. A comprehensive study of pristine, fine-grained spinel-rich

inclusions from the Leoville and Efremovka CV3 chondrites I: petrology. Lunar Planet. Sci. 33 CD-ROM #1526.

McSween, H.Y., 1977. Chemical and petrographic constraints on the origin of chondrules and inclusions in carbonaceous chondrites. Geochim. Cosmochim. Acta 41, 1843−1860.

Osborn, E.F., Tait, D.B., 1952. The system diopside−forsterite−anorthite. Am. J. Sci. Bowen volume, 413−433.

Petaev, M.I., Wood, J.A., 2005. Meteoritic constraints on temperatures, pressures, cooling rates, chemical compositions, and modes of condensation in the solar nebula. In: Krot, A.N., Scott, E.R.D. (Eds.), Chondrules and the Protoplanetary Disk ASP Conference Series 341, pp. 373−406.

Petaev, M.I., Krot, A.N., Wood, J.A., 2005. Nebular condensation under incomplete equilibrium: implications for the fine-grained spinel-rich CAIs. Lunar Planet. Sci. 36 CD-ROM #1238.

Radomsky, P.M., Hewins, R.H., 1990. Formation conditions of pyroxene-olivine and magnesian olivine chondrules. Geochim. Cosmochim. Acta 54, 3475−3490.

Rubin, A.E., 1998. Correlated petrologic and geochemical characteristics of CO3 chondrites. Meteorit. Planet. Sci. 33, 385−391.

Shu, F.H., Shang, H., Gounelle, M., Glassgold, A.E., Lee, T., 2001. The origin of chondrules and refractory inclusions in chondritic meteorites. Astrophys. J. 548, 1029−1070.

Spencer, J.P., Humphrey, C.J., Hirsh, P.B., 1972. A dynamical theory for the contrast of perfect and imperfect crystals in the scanning electron microscope using backscattered electrons. Philos. Mag. 26, 192−213.

Stolper, E., Paque, J.M., 1986. Crystallization sequences of Ca−Al-rich inclusions from Allende: the effects of cooling rate and maximum temperature. Geochim. Cosmochim. Acta 50, 1785−1806.

Sugiura, N., Miyazaki, A., Hiyagon, H., Kimura, M., Petaev, M.I., 2006. Nebular history of amoeboid olivine aggregates. Lunar Planet. Sci. 37 CD-ROM #1266.

Weisberg, M.K., Conolly Jr., H.C., Ebel, D.S., 2004. Petrology and origin of amoeboid olivine aggregates in CR chondrites. Meteorit. Planet. Sci. 39, 1741−1753.

Wood, A.J., Hashimoto, A., 1993. Mineral equilibrium in fractionated nebular systems. Geochim. Cosmochim. Acta 57, 2377−2388.

Yoneda, S., Grossman, L., 1995. Condensation of CaO−MgO−Al_2O_3−SiO_2 liquids from cosmic gases. Geochim. Cosmochim. Acta 59, 3413−3444.